

Supporting Information

Atomically dispersed iridium catalysts for multifunctional electrocatalysis

Qiaoqiao Zhang,^{a,#} Zhiyao Duan,^{b,#,*} Yin Wang,^{c,#} Lina Li,^{d,*} Bing Nan,^d and Jingqi

Guan^{a,*}

^aKey Laboratory of Surface and Interface Chemistry of Jilin Province, College of Chemistry, Jilin University, Changchun 130012, PR China.

*E-mail: guanjq@jlu.edu.cn (J. Guan)

^bDepartment of Chemistry and Oden Institute for Computational Engineering and Sciences, The University of Texas at Austin, Austin, TX, 78712-1224, USA.

*E-mail: zhiyao.duan@cm.utexas.edu (Z. Duan)

^cInner Mongolia Key Laboratory of Carbon Nanomaterials, College of Chemistry and Chemical Engineering, Nano Innovation Institute, Inner Mongolia University for Nationalities, Tongliao 028000, China.

^dShanghai Synchrotron Radiation Facility, Shanghai Advanced Research Institute, Shanghai, 201204, China.

*E-mail: lilina@sinap.ac.cn (L. Li)

#These authors contributed equally to this work.

Experimental section

Synthesis of 0.7-Ir@G-750 and 0.7-Ir@NG-750

Graphene oxide (GO) was first prepared according to a modified Hummer's method.¹ 0.2 g GO and 2.5 mg IrCl₃·3H₂O (Ir/GO = 0.7 wt.%) was dispersed in 50 mL H₂O by ultrasonic for 1.0 h. Then, the mixture was poured into liquid nitrogen. After the water was removed by a freeze-drying equipment, the residual yellow solid was annealed at 750 °C under an ammonia atmosphere for 2 hours to obtain black 0.7-Ir@NG-750.

For comparison, c-Ir@NG-T (c: initial iridium content, T: annealing temperature) with different initial iridium content (i.e. 0.1 wt.%, 0.3 wt.%, 0.5 wt.%, 0.7 wt.%, 0.9 wt.%, and 1.1 wt.%) and different annealing temperature (i.e. 450 °C, 550 °C, 650 °C, 750 °C, and 850 °C) was prepared by a similar synthetic procedure with the above synthesis except the different initial Ir content and different annealing temperature. In addition, 0.7-Ir@G-750 was prepared by annealing the precursor of IrCl₃/GO at 750 °C under an Ar atmosphere for 2 hours. G and NG was prepared by annealing GO at 750 °C under an Ar atmosphere and an ammonia atmosphere for 2 hours, respectively. The absolute yield of 0.7 wt.%-Ir@NG-750 is ca. 90 mg.

Material characterizations

Raman spectra were recorded on a Raman spectrometer (Renishaw, Inc.) using a 532 nm laser source. Transmission electron microscope (TEM) images were observed by a Hitachi HT7700. High angle annular dark field imaging (HAADF) was

performed with an aberration-corrected JEM-ARM 200F microscope. The valence state of manganese was determined using XPS recorded on a Thermo ESCALAB 250Xi. The X-ray source selected was monochromatized Al K_{α} source (15 kV, 10.8 mA). Region scans were collected using a 20 eV pass energy. Peak positions were calibrated relative to C 1s peak position at 284.6 eV. The loading amount of iridium in the catalysts was determined using inductively coupled plasma atomic emission spectrometer (ICP-AES) on a Shimadzu ICPS-8100. Prior to ICP-AES measurement, 50 mg sample was placed in a 50 mL beaker and calcined in an oven at 520 °C for 6 h to completely remove the carbon. The residue was dissolved in aqua regia and diluted with water to test the iridium content.

The X-ray absorption fine structure (XAFS) spectra at Ir L₃ ($E_0 = 11215$ eV) edge were performed at 11B beamline of Shanghai Synchrotron Radiation Facility (SSRF) operated at 3.5 GeV under “top-up” mode with a constant current of 240 mA. The XAFS data were recorded under fluorescence mode with a Lytle detector. The energy was calibrated accordingly to the absorption edge of pure Ir powder. Athena and Artemis codes were used to extract the data and fit the profiles. For the X-ray absorption near edge structure (XANES) part, the experimental absorption coefficients as function of energies $\mu(E)$ were processed by background subtraction and normalization procedures, and reported as “normalized absorption”. For the extended X-ray absorption fine structure (EXAFS) part, the Fourier transformed (FT) data in R space were analyzed by applying first-shell approximate model for Ir-O/N contribution. The passive electron factor, S_0^2 , was determined by fitting the experimental data on Ir foil and fixing the coordination number (CN) of Ir-Ir for further analysis of the measured samples. The parameters describing the

electronic properties (e.g., correction to the photoelectron energy origin, E_0) and local structure environment including CN , bond distance (R) and Debye-Waller ($D.W.$) factor around the absorbing atoms were allowed to vary during the fit process. The fitted range for k space was selected to be $k = 3\text{-}10 \text{ \AA}^{-1}$ (k^2 weighted).

Electrochemical activity characterizations

All electrochemical measurements were performed in a three-electrode system with a glassy carbon electrode (GCE) as the substrate for the working electrode, a graphite rod as the counter electrode and a saturated calomel electrode as the reference electrode. The reference electrode was calibrated with respect to a reversible hydrogen electrode before each experiment. The glassy carbon electrode was pre-polished using $0.05 \mu\text{m}$ alumina and distilled water. To prepare the working electrode, 2 mg of the catalyst was dispersed in a 0.5 mL mixed solvent of ethanol and Nafion (0.25 wt%) and sonicated to obtain a homogeneous ink. 5 μL of the catalyst ink was drop-casted on the glassy carbon electrode and dried at room temperature (catalyst loading: $0.28 \text{ mg}\cdot\text{cm}^{-2}$). For simplicity, all overpotential, Tafel slope and current density values in this manuscript are represented as positive quantities.

For OER, the working electrode was first activated by steady-state cyclic voltammetry (CV) performed in the potential range from 1.0 to 1.6 V vs RHE at a scan rate of 50 mV s^{-1} for 50 cycles. Linear scan voltammetry (LSV) curves were then collected at a scan rate of 5 mV s^{-1} . All of the potentials in the LSV polarization curves were without iR compensation unless specifically illustrated.

For ORR, the CV experiments were performed in N₂/O₂ saturated 0.1 M KOH or 0.5 M H₂SO₄ at room temperature with a scan rate of 5 mV s⁻¹. Ring-disk electrode (RDE) tests were performed in O₂ saturated 0.1 M KOH or 0.5 M H₂SO₄ with a scan rate of 5 mV s⁻¹. The electron transfer number during ORR was calculated by Koutecky–Levich equation:

$$\frac{1}{J} = \frac{1}{J_K} + \frac{1}{J_L} = \frac{1}{J_K} + \frac{1}{B\omega^{1/2}} \quad (1)$$

$$B = n \cdot F \cdot (D_0)^{2/3} \cdot v^{-1/6} \quad (2)$$

where J is the measured current density, J_K and J_L are the kinetic and diffusion-limiting current densities, ω is the angular velocity, n is transferred electron number, F is Faraday constant (96485 C mol⁻¹), C_0 is the bulk concentration of O₂ (1.2 × 10⁻⁶ mol cm⁻³), D_0 is the diffusion coefficient of O₂ in 0.1 M KOH (1.9 × 10⁻⁵ cm² s⁻¹), and v is the kinetic viscosity of the electrolyte (0.01 cm² s⁻¹).

Computational methods

Density functional theory

Spin-polarized DFT calculations were performed using the Vienna Ab initio Simulation Package.^{2, 3} The generalized gradient approximation with the PBE functional was used to describe the exchange and correlation energy.⁴ Electron–ion interactions were treated by the projector augmented wave method.⁵ In all calculations, the energy cutoff of the plane-wave basis set was 400 eV. The DFT+U method was applied to 3d orbitals of Fe to correct the on-site Coulomb interactions.⁶ A value of U_{eff} = 5 eV was used to reproduce the electronic structure that has been observed

experimentally.⁷ Brillouin zone was sampled by Monkhorst-Pack k-point meshes.⁸ Optimized structures were obtained by minimizing the forces on each ion until they fell below 0.05 eV/Å. The solvation effects were also considered using an implicit solvation model implemented in VASP.⁹ The relative permittivity for the continuum solvent was set to 80 to simulate a water environment.

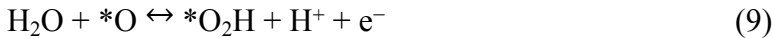
Computational hydrogen electrode

Thermochemistry of the electrochemical oxygen reduction reaction (ORR), oxygen evolution reaction (OER), and hydrogen evolution reaction (HER) was calculated by applying the computational hydrogen electrode method.¹⁰ This method has previously proved successful in predicting ORR and OER activity trends on various catalysts.¹⁰⁻¹³ Briefly, the Gibbs free energy change of each electrochemical elementary step of the ORR and OER was calculated with DFT. The ORR reaction mechanism was assumed to follow the four-step associative mechanism represented in eqs 3-6.

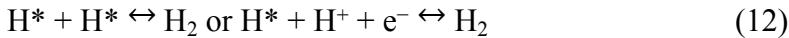


The OER reaction mechanism was assumed to follow the four-step mechanism represented in eqs 7-10.





The reaction mechanism of HER is represented in eqs 11-12.



The free energy change of each elementary steps can be calculated as $\Delta G = \Delta E - T\Delta S + \Delta ZPE$, where ΔZPE is the zero-point energy. The total energy changes (ΔE) of these elementary steps are the energy differences between DFT-calculated energies of reactant and product states. Here, for both ORR and OER, we evaluated the binding energies of OH^* , O^* , and OOH^* on the surfaces of the catalysts under consideration. The chemical potential of the solvated proton and electron pair ($\text{H}^+ + \text{e}^-$) at standard conditions ($\text{pH}=0$, $T=298.15$ K) is calculated as $1/2G_{\text{H}_2} + eU_{\text{SHE}}$ assuming equilibrium at the standard hydrogen electrode. The changes in ΔZPE and $T\Delta S$ are calculated using previously determined values.⁵⁴ With this approach, the theoretical overpotential of OER (η^{OER}) at standard conditions is defined as:

$$\eta^{\text{OER}} = (G^{\text{OER}}/e) - 1.23 \text{ V} \quad (13),$$

where G^{OER} is the potential determining step defined as the highest free energy step in the process of OER. Similarly, the theoretical overpotential of ORR (η^{ORR}) is defined as:

$$\eta^{\text{ORR}} = 1.23 \text{ V} - (G^{\text{ORR}}/e) \text{ V} \quad (14).$$

The theoretical overpotential of HER (η^{HER}) is defined as:

$$\eta^{\text{ORR}} = |\Delta G_{\text{H}^*}/e| \text{ V} \quad (15),$$

where ΔG_{H^*} is the free energy of hydrogen adsorption at equilibrium potential of HER at standard conditions.

Double reference method

The double reference method was used to simulate the electric double layer (EDL) and determine the binding energies of reaction intermediates under constant-potential conditions.¹⁴ Our approach is different from the original implementation of the double reference method,¹⁴ where explicit water molecules are used to model the metal/aqueous interface. Here, the aqueous environment is treated by the continuum solvation model developed by Hennig and coworkers as implemented in the VASPsol code.⁹ The relative permittivity of the solvent was set to $\epsilon_{\text{solv}} = 80$ to account for the presence of the aqueous electrolyte. This value corresponds to the permittivity of bulk water.

Details of the double reference method can be found elsewhere.^{15, 16} Briefly, the electric potential of the simulated electrochemical interface is varied by changing the number of electrons in the system. To maintain charge neutrality of the super cell, a uniform background of compensating counter charge was added. The charged slab, together with the compensating background charge, polarizes the electrolyte near the metal/solution interface thereby creating an electrostatic potential profile that simulates the EDL.

For each electrochemical interface, DFT calculations were performed at various

charges by inserting or deleting electrons from the simulated system. The total free energy at each point was then fit to a quadratic equation to provide a continuous free energy as a function of potential. The quadratic form is consistent with a capacitor created by the charged-slab/background-charge system, which takes the form of eq 16.

$$E(U) = -\frac{1}{2}C(U - U_{\text{pzc}})^2 + E_0 \quad (16)$$

Here, U_{pzc} refers to the potential of zero charge (PZC), E_0 is the energy at the PZC, and C is the capacitance of the metal/aqueous interface. From the quadratic equations fit for the bare slab and adsorption models, the binding energies as a function of electric potential are readily calculated.

Calibration of SCE and conversion to RHE

The reference electrode SCE was calibrated according to the method reported previously.¹⁷⁻¹⁹ Calibrations were carried out by using a reversible hydrogen electrode (RHE). First, two Pt electrodes were cleaned by cycling in 1 M H₂SO₄ between -2 and 2 V for 2 hours. Then, they were used as working electrode and counter electrode, respectively. Before the calibration, the electrolytes 0.1 M KOH and 0.5 M H₂SO₄ should be saturated with H₂ by continuous bubbling H₂. During the calibration, hydrogen was bubbled over the working electrode. A series of controlled-potential chronoamperometric curves were measured for 300 s to get the current interconvert between the hydrogen oxidation and hydrogen evolution reaction. The resulting potential is the potential of zero net current. In this work, the potential of zero net current was found at -1.038 V versus the SCE electrode in 1.0 M KOH, -1.003 V versus the SCE electrode in 0.1 M KOH, and -0.253 V versus the SCE electrode in 0.5 M H₂SO₄. Thus, the potentials, measured against SCE, were converted into the potentials versus RHE by using the equations 17-19:

$$\text{In 1.0 M KOH: } E_{\text{vs.RHE}} = E_{\text{vs.SCE}} + 1.038 \text{ V} \quad (17)$$

$$\text{In 0.1 M KOH: } E_{\text{vs.RHE}} = E_{\text{vs.SCE}} + 1.003 \text{ V} \quad (18)$$

$$\text{In 0.5 M H}_2\text{SO}_4: E_{\text{vs.RHE}} = E_{\text{vs.SCE}} + 0.253 \text{ V} \quad (19)$$

Electrochemically active surface area (ECSA)

To determine the effective electrochemical active surface area (ECSA) of samples, a series of cyclic voltammetry (CV) curves were tested at various scan rates (10, 20, 40, 60, 80 and 100 mV/s) in the potential window between 0.188 and 0.288 V vs. RHE. The sweep segments of the measurements were set to 10 to ensure consistency. The geometric double layer capacitance (C_{dl}) was calculated by plotting the difference of current density $\Delta J = (J_{anodic} - J_{cathodic})/2$ at 0.238 V vs. RHE against the scan rate, and the slope of the linear trend was C_{dl} . Finally, the ECSA of catalyst on GCE is estimated according to the equation 20:

$$ECSA = \frac{C_{dl}}{C_s} \quad (20)$$

where C_s is the specific capacitance of a flat standard electrode with 1 cm² of real surface area, which is generally in the range of 20 to 60 μF cm⁻².^{20, 21} In this work, the averaged value of 40 μF cm⁻² was adopted for the flat electrode.

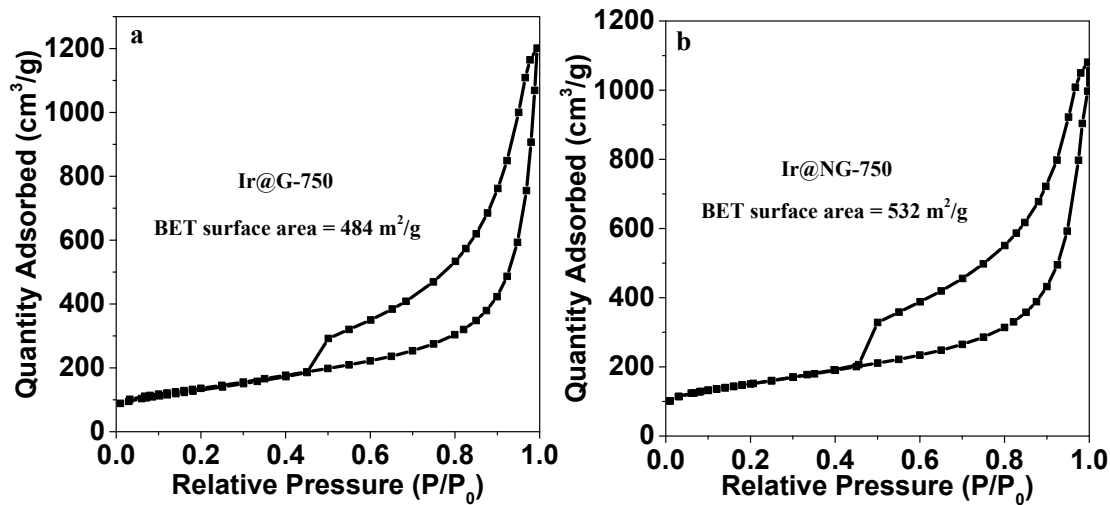


Figure S1. N₂ adsorption–desorption isotherms of Ir@G-750 and Ir@NG-750.

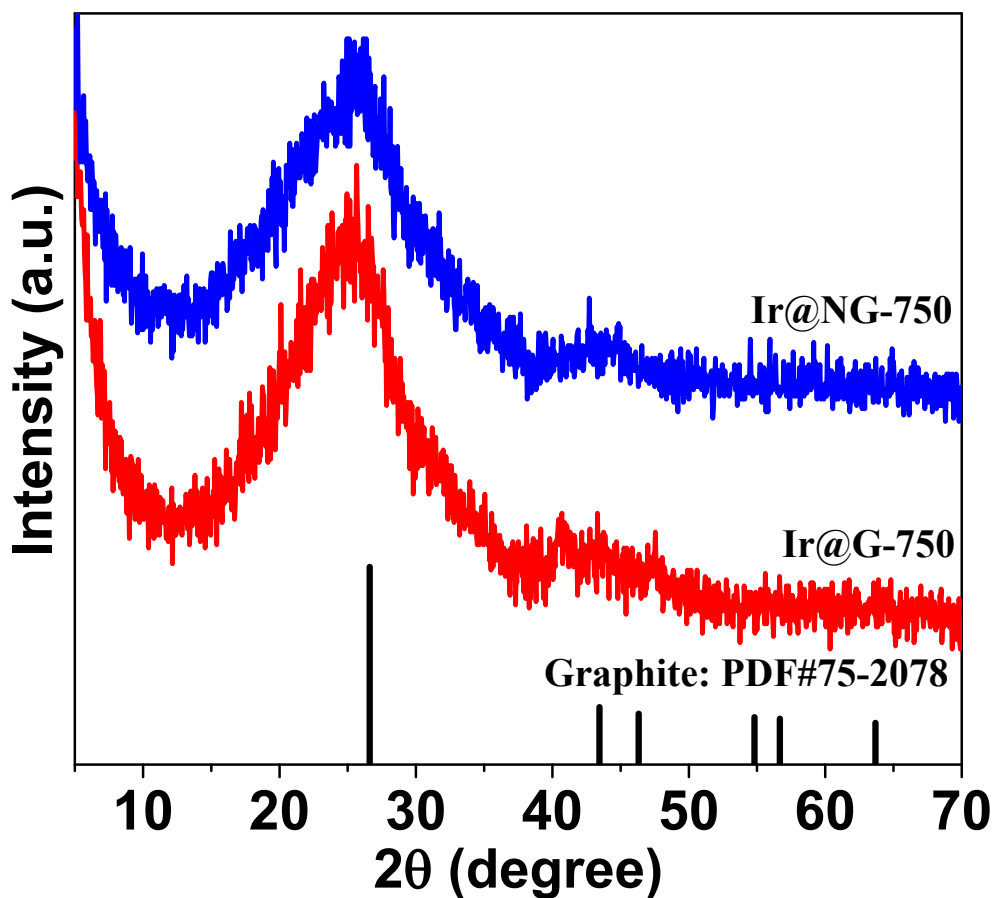


Figure S2. Powder X-ray diffraction (XRD) patterns of Ir@G-750 and Ir@NG-750.

Reference code for graphite: JCPDS #75-2078. No peaks attributed to Ir/IrO_x nanoparticles were detected.

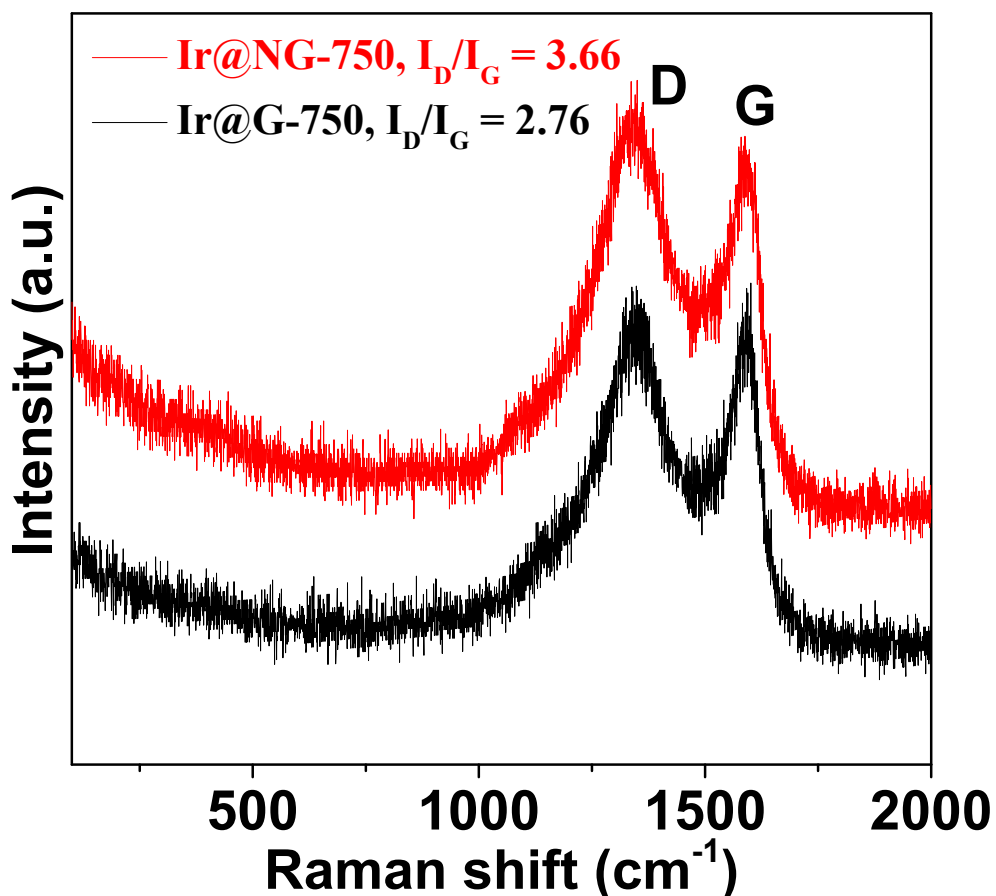


Figure S3. Raman spectra of Ir@G-750 and Ir@NG-750. No obvious peaks attributed to Ir/IrO_x nanoparticles were detected.

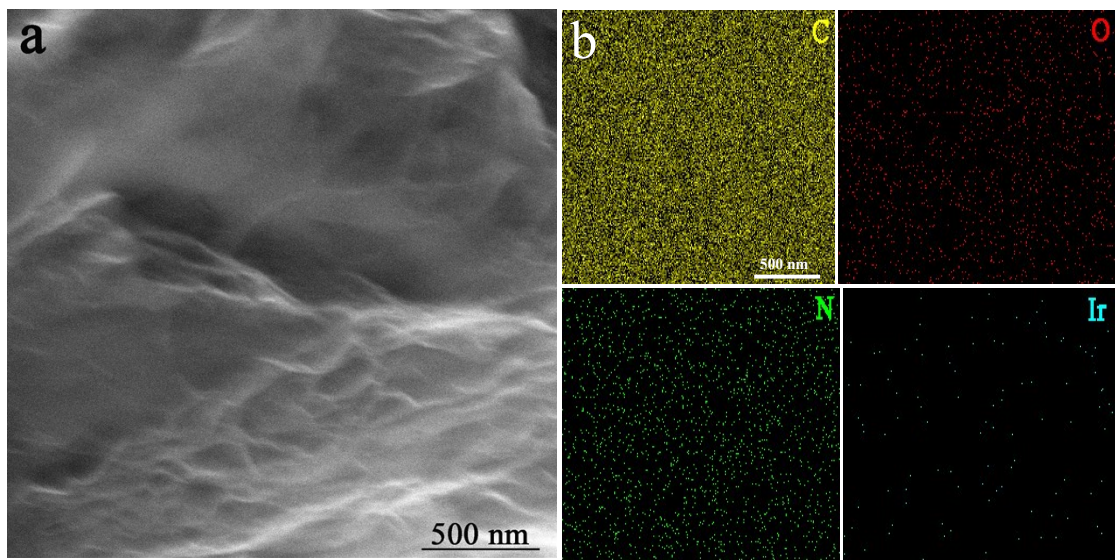


Figure S4. (a) SEM image used in the EDS mapping test, and (b) the corresponding EDS mapping of Ir@NG-750.

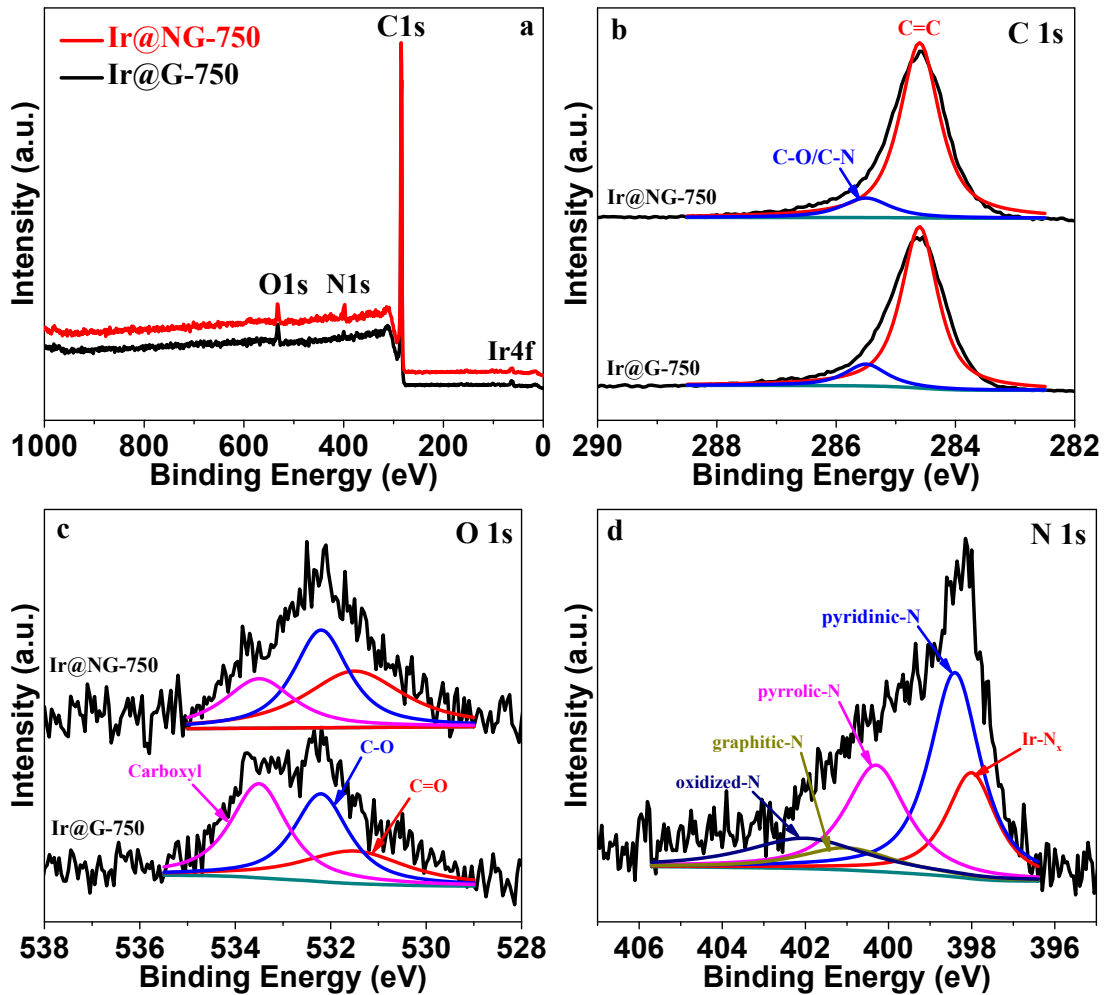


Figure S5. (a) XPS survey spectra, (b) high-resolution XPS spectra of C1s. and (c) high-resolution XPS spectra of O1s for Ir@G-750 and Ir@NG-750. (d) High-resolution XPS spectrum of N1s for Ir@NG-750.

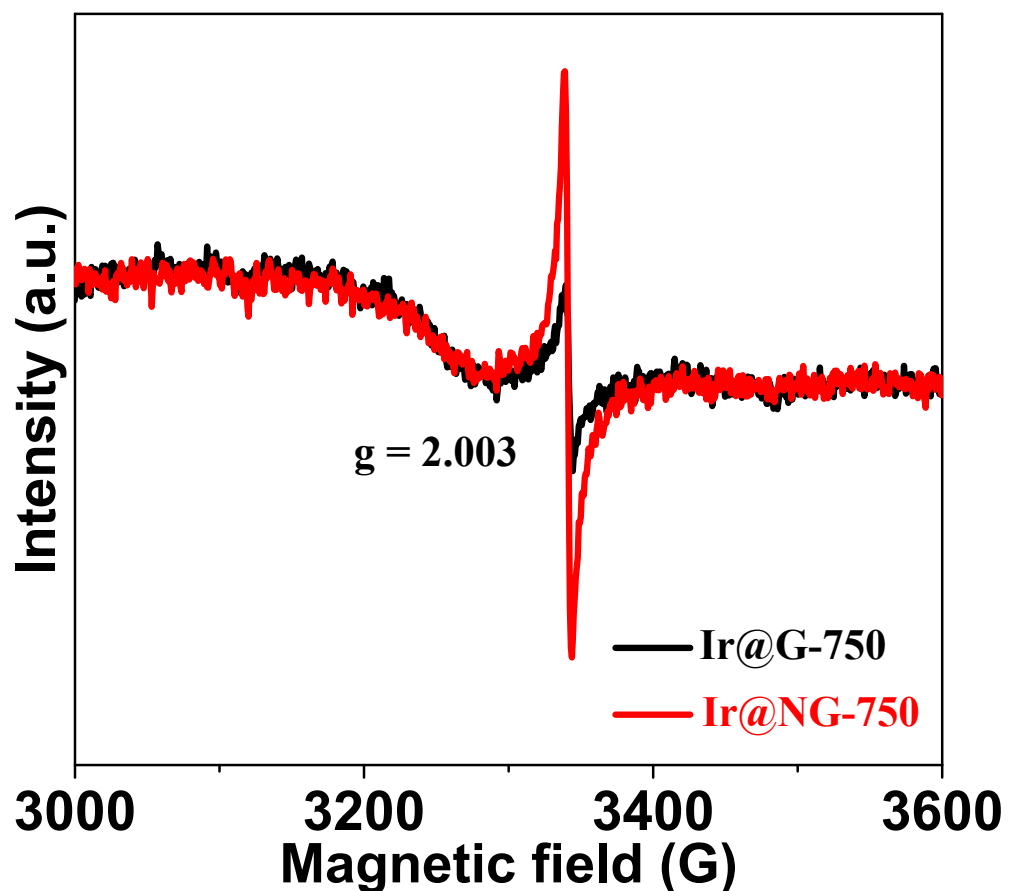


Figure S6. EPR spectra of Ir@G and Ir@NG.

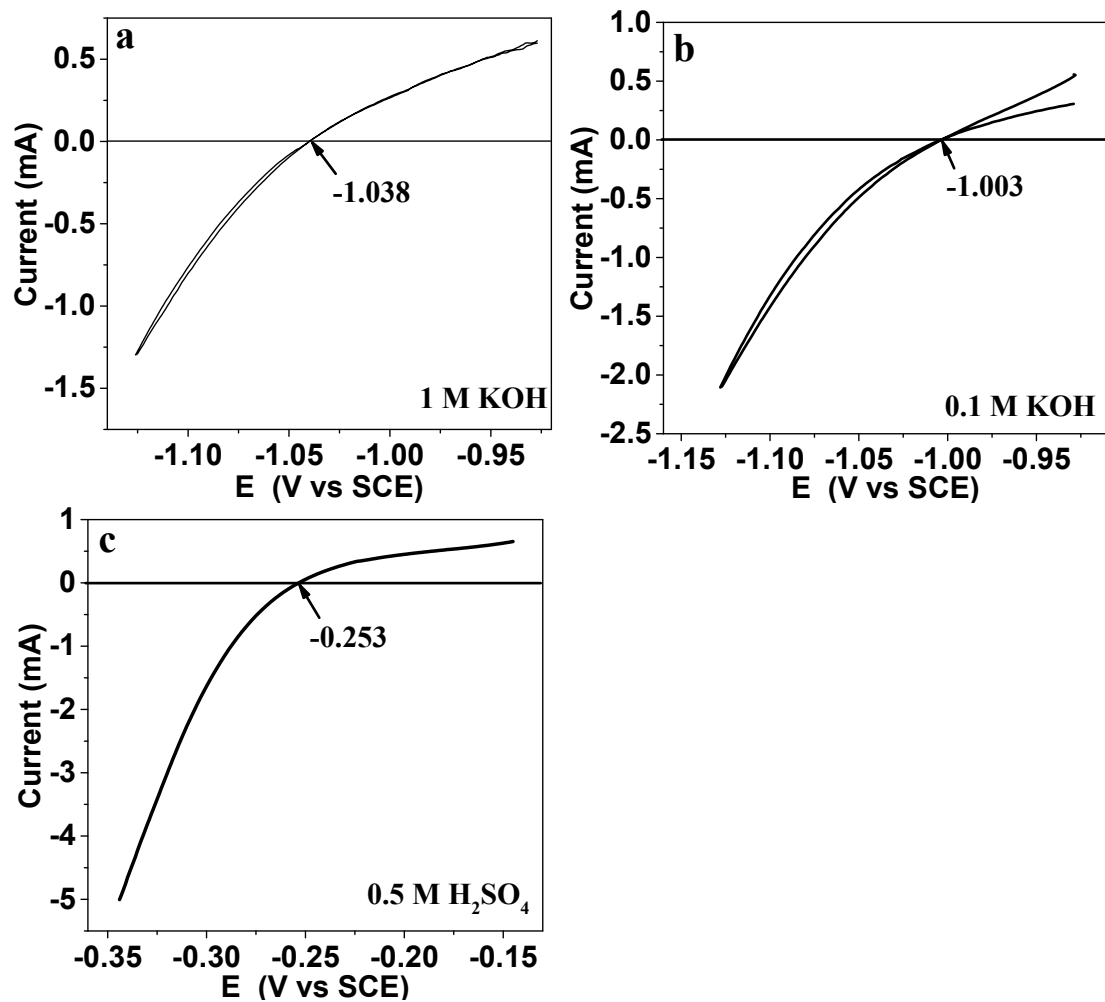


Figure S7. The current as a function of the applied potentials for the calibration of SCE reference electrode in 1.0 M KOH (a), 0.1 M KOH (b) and 0.5 M H₂SO₄ (c).

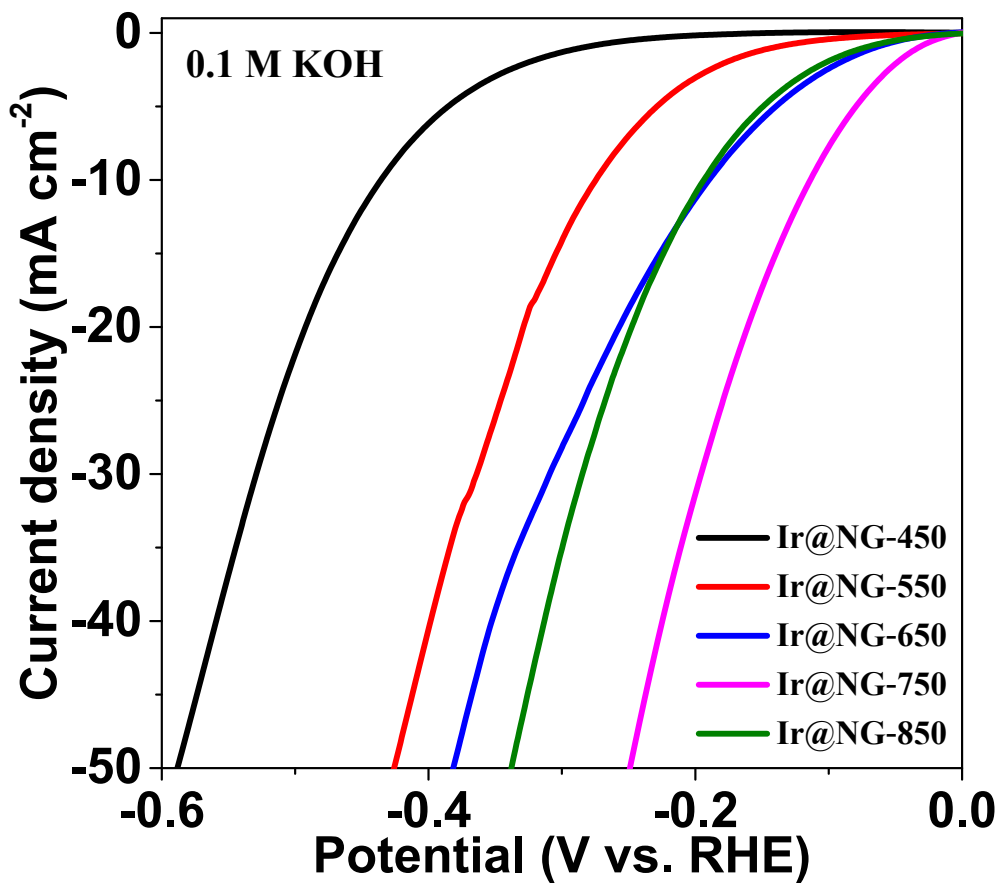


Figure S8. LSV curves of 0.7-Ir@NG-T with different annealing temperature in 0.1 M KOH.

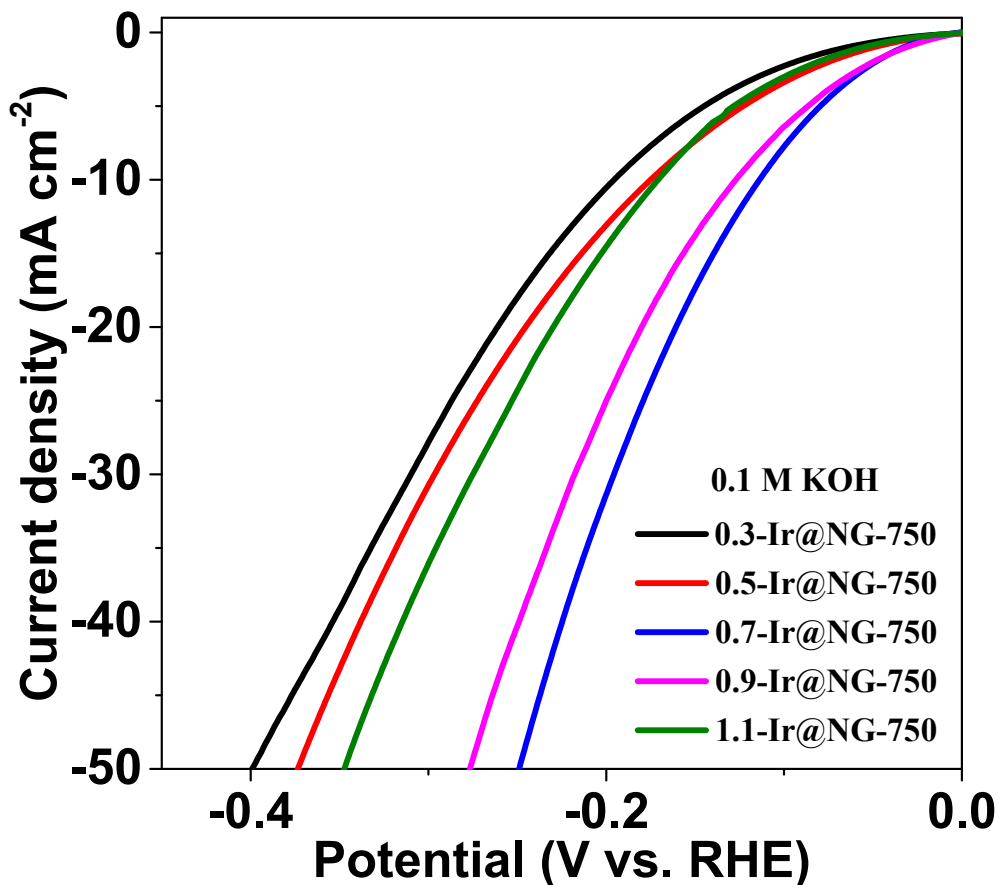


Figure S9. LSV curves of Ir@NG-750 with different initial Ir content in 0.1 M KOH.

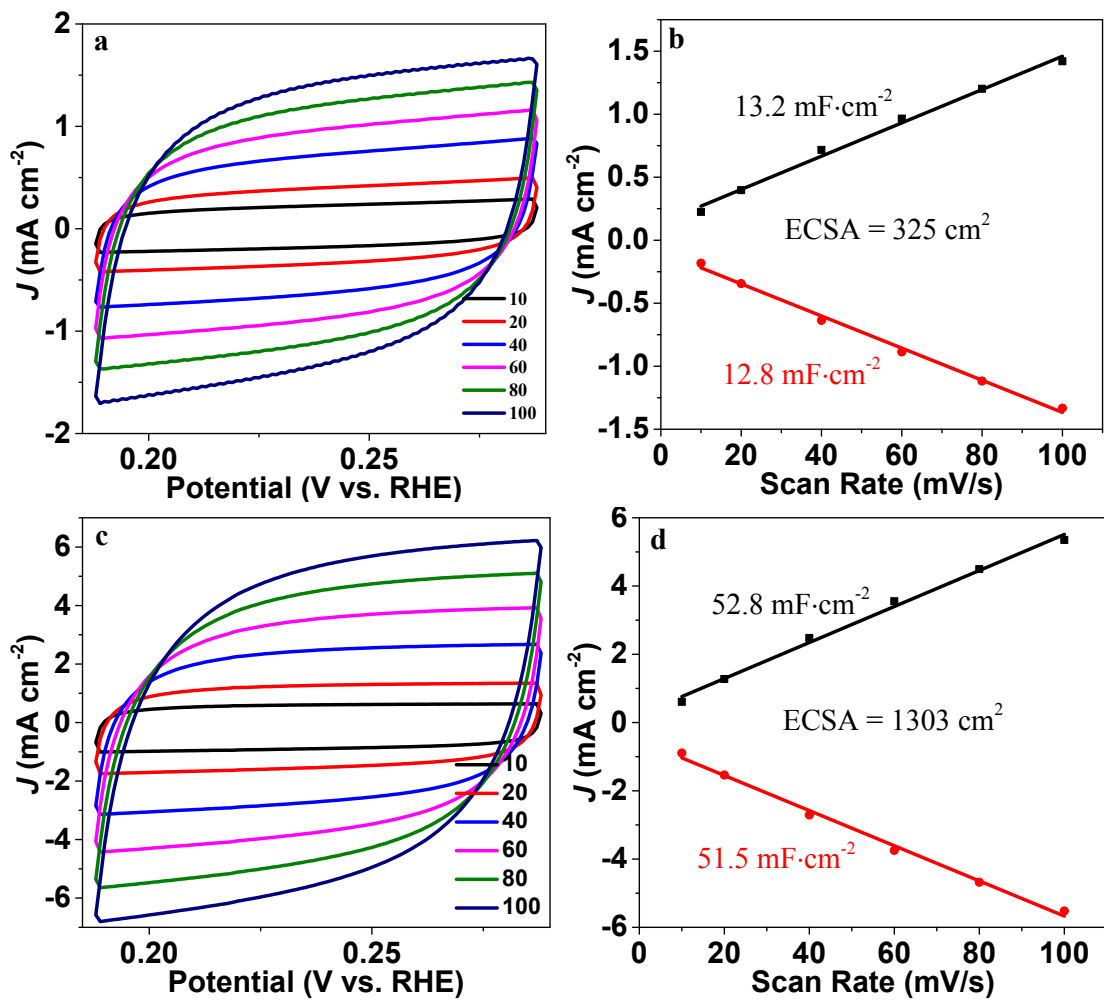


Figure S10. Double-layer capacitance measurements for determining the electrochemical active surface area for the Sc@G-750 (a, b) and Sc@NG-750 (c, d). (a, c) CVs measured in a non-Faradaic region at scan rate of 10 mV s^{-1} , 20 mV s^{-1} , 40 mV s^{-1} , 60 mV s^{-1} , 80 mV s^{-1} , and 100 mV s^{-1} . (b, d) The cathodic (black) and anodic (red) currents measured at 0.238 V vs RHE as a function of the scan rate. The average of the absolute value of the slope is taken as the double-layer capacitance of the electrode.

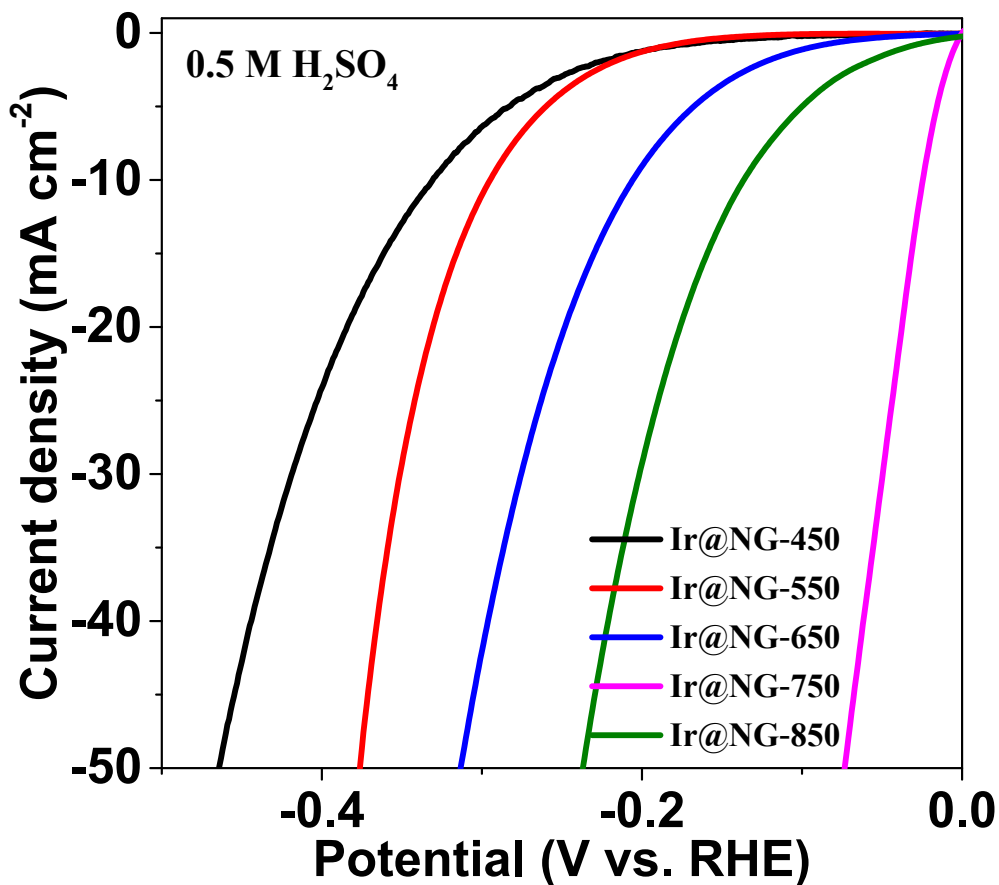


Figure S11. LSV curves of 0.7-Ir@NG-T with different annealing temperature in 0.5 M H_2SO_4 .

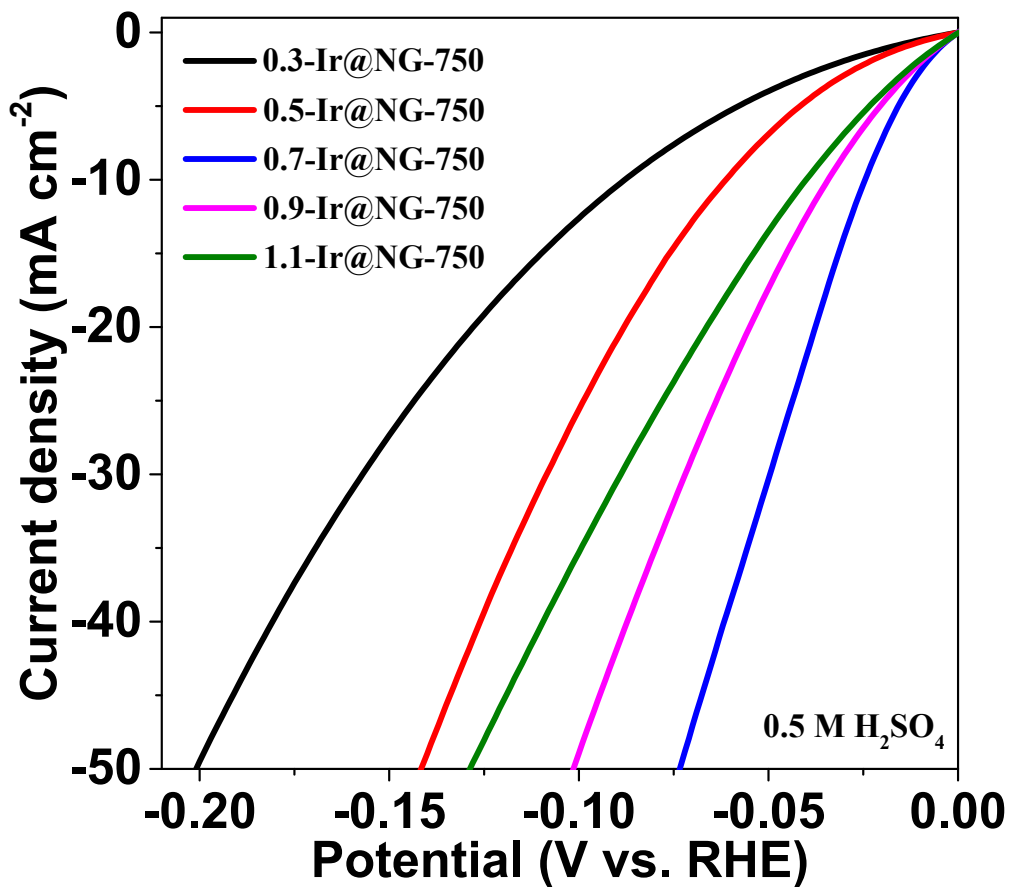


Figure S12. LSV curves of Ir@NG-750 with different initial Ir content in 0.5 M H_2SO_4 .

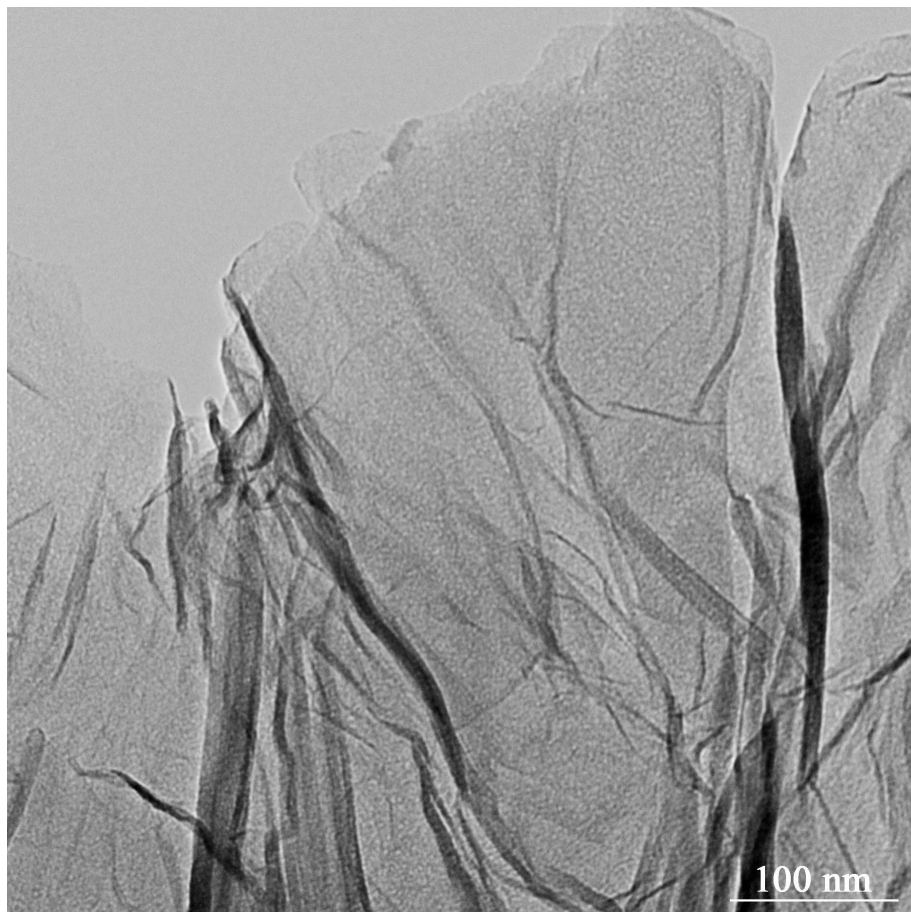


Figure S13. TEM image of the Ir@NG-750 after the HER stability test.

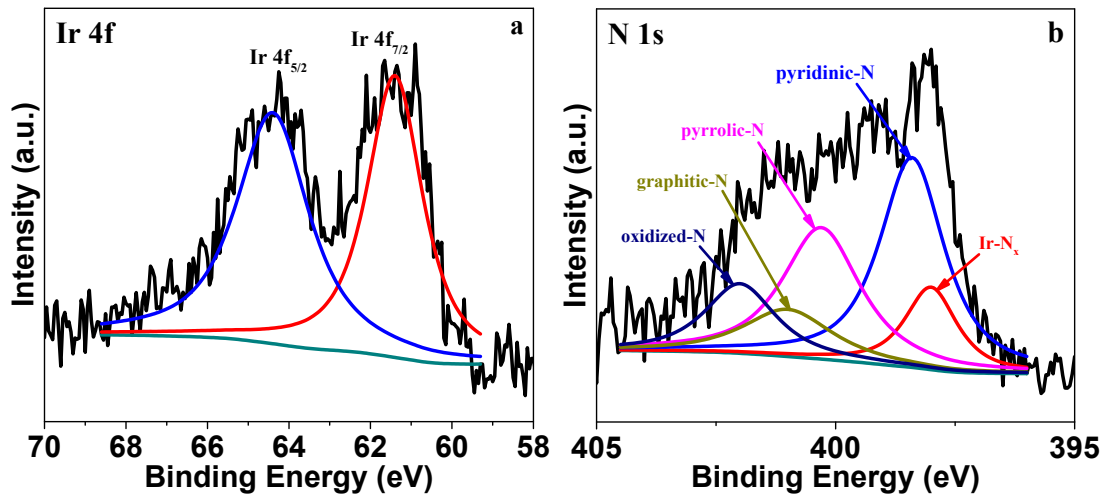


Figure S14. The high-resolution Ir4f (a) and N1s (b) XPS spectra of the used Ir@NG-750 catalyst after HER test in 0.5 M H₂SO₄.

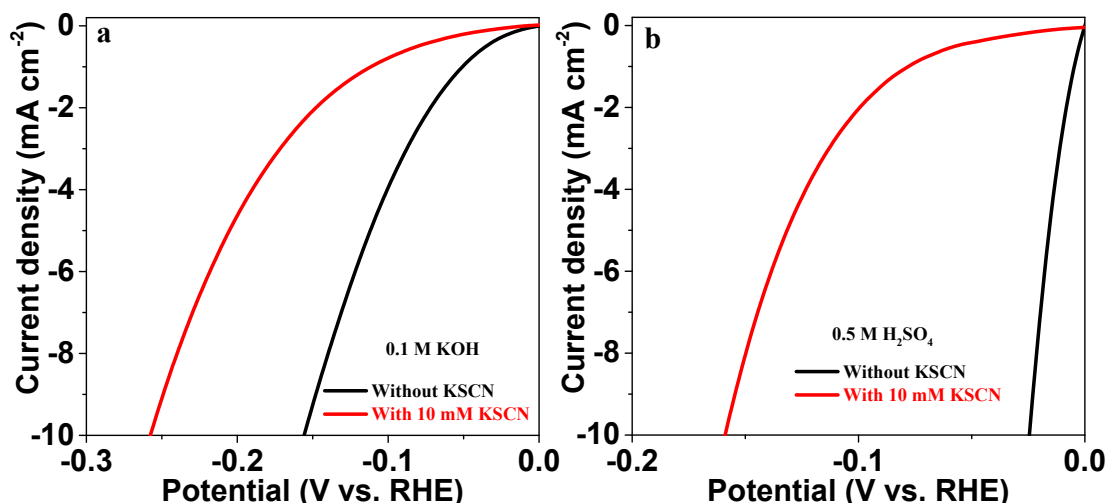


Figure S15. LSV polarization curves for HER on Ir@NG-750 in 0.1 M KOH and 0.5 M H_2SO_4 (b) with and without 10 mM KSCN.

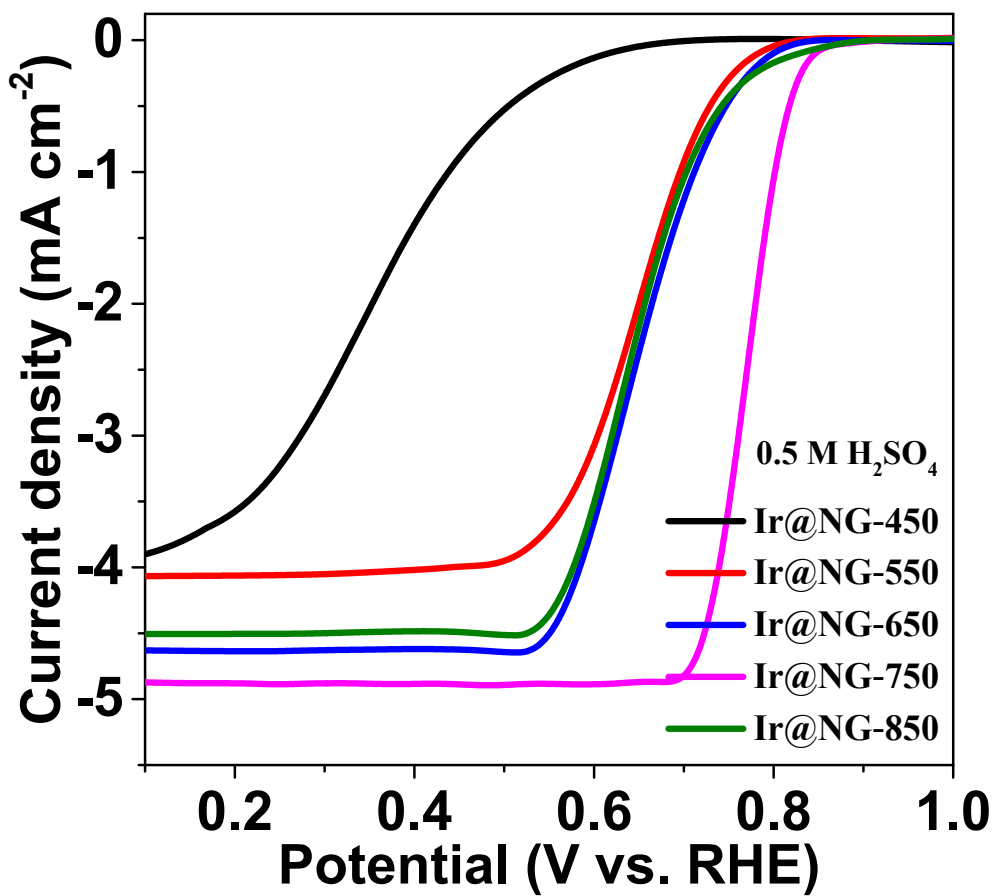


Figure S16. Polarization curves of 0.7-Ir@NG-T with different annealing temperature

at a rotation speed of 1600 rpm in 0.5 M H_2SO_4 .

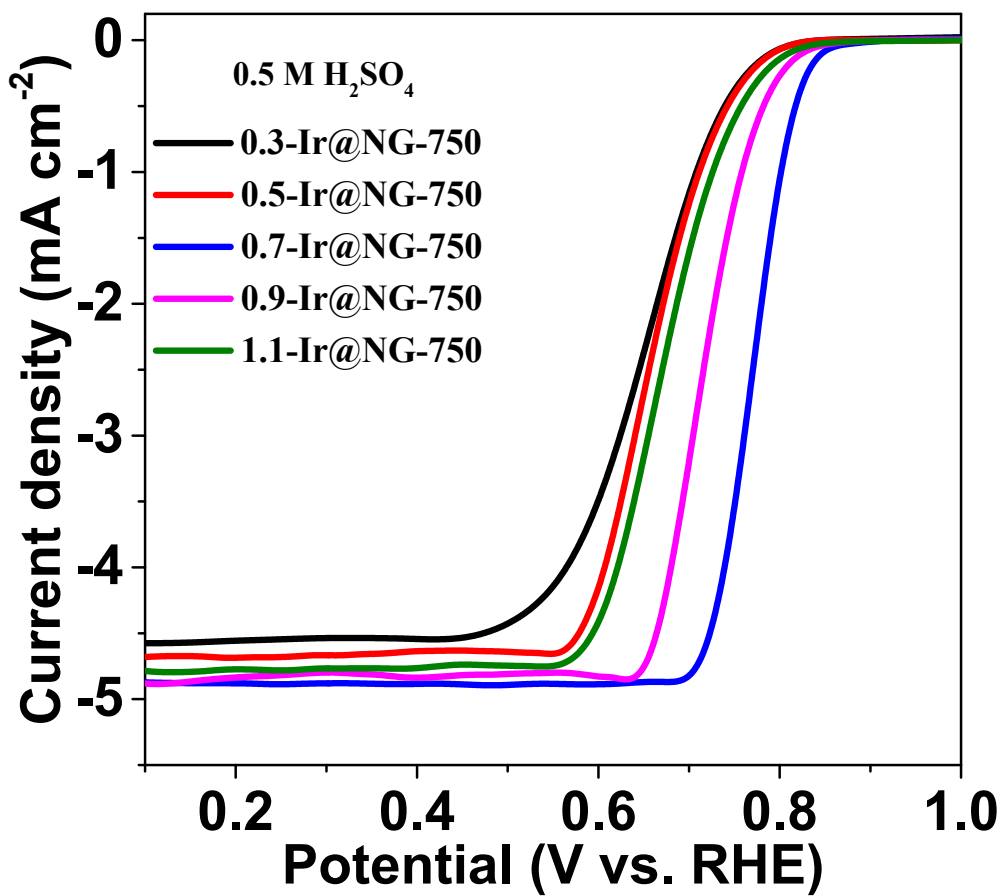


Figure S17. Polarization curves of Ir@NG-750 with different initial Ir content at a rotation speed of 1600 rpm in 0.5 M H_2SO_4 .

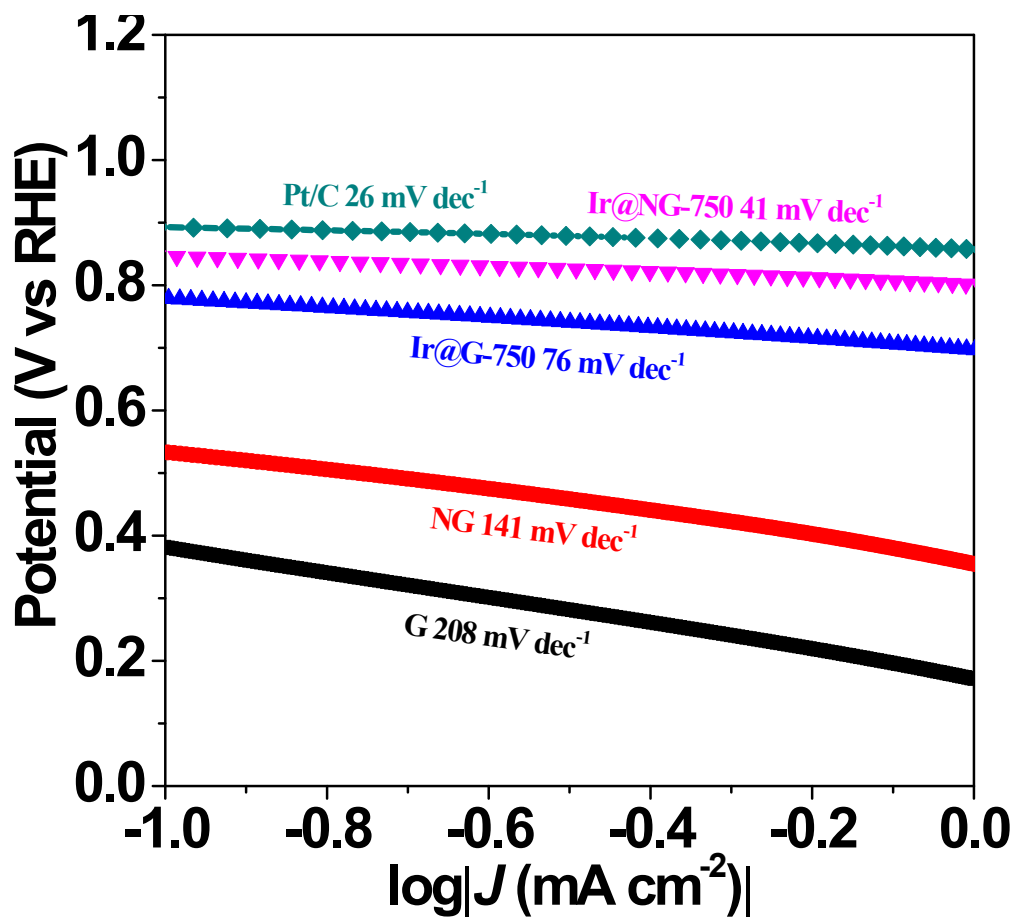


Figure S18. Tafel plots for Pt/C, G, NG, Ir@G-750, and Ir@NG-750 in 0.5 M H_2SO_4 .

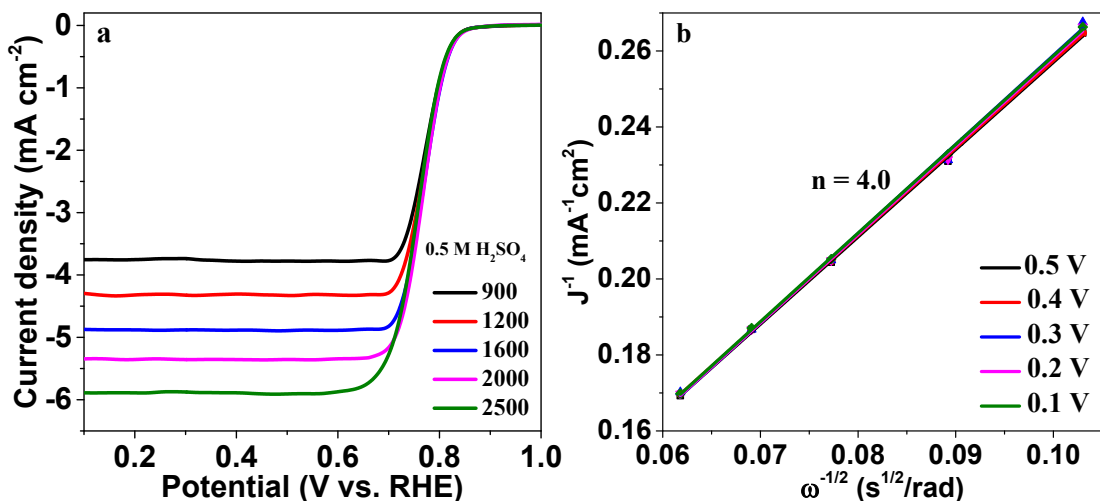


Figure S19. (a) Polarization curves of Ir@NG-750 at various rotation speeds in O_2 -saturated $0.5 \text{ M H}_2\text{SO}_4$. (b) The corresponding Koutecky–Levich plots.

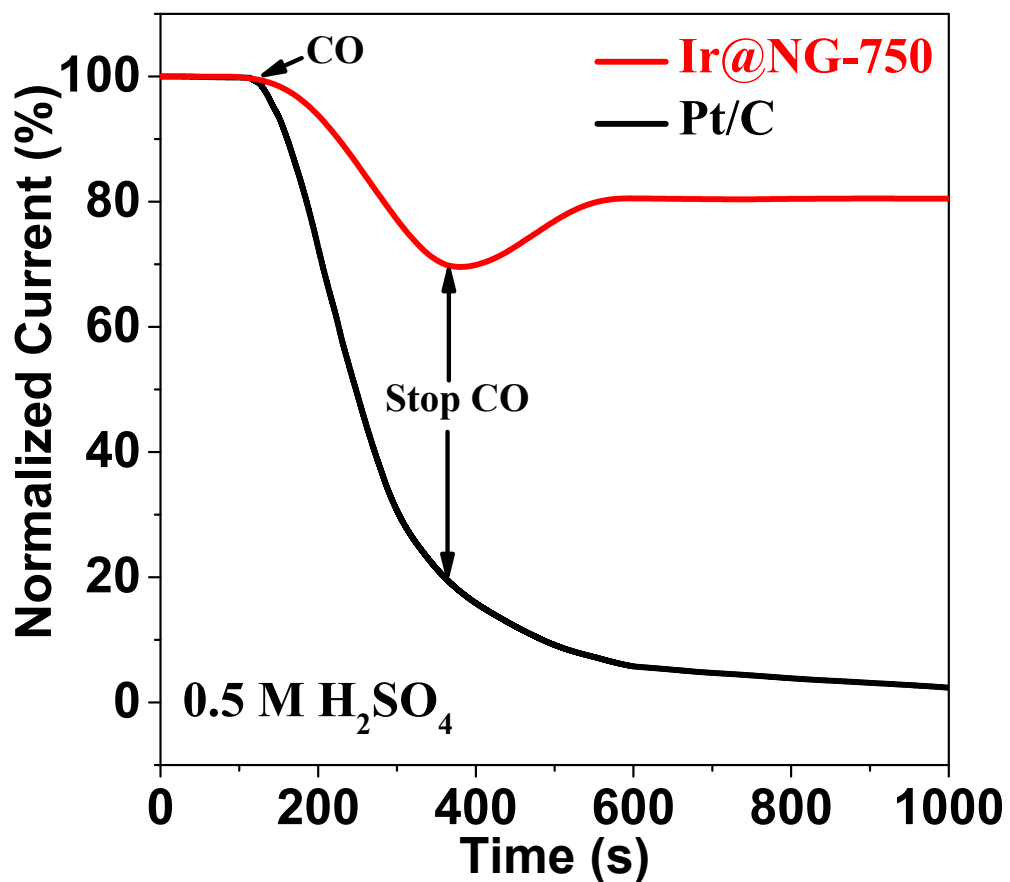


Figure S20. Tolerance to carbon monoxide of Ir@NG-750 compared with 20 wt% Pt/C in O₂-saturated 0.5 M H₂SO₄ solution at 0.6 V vs RHE.

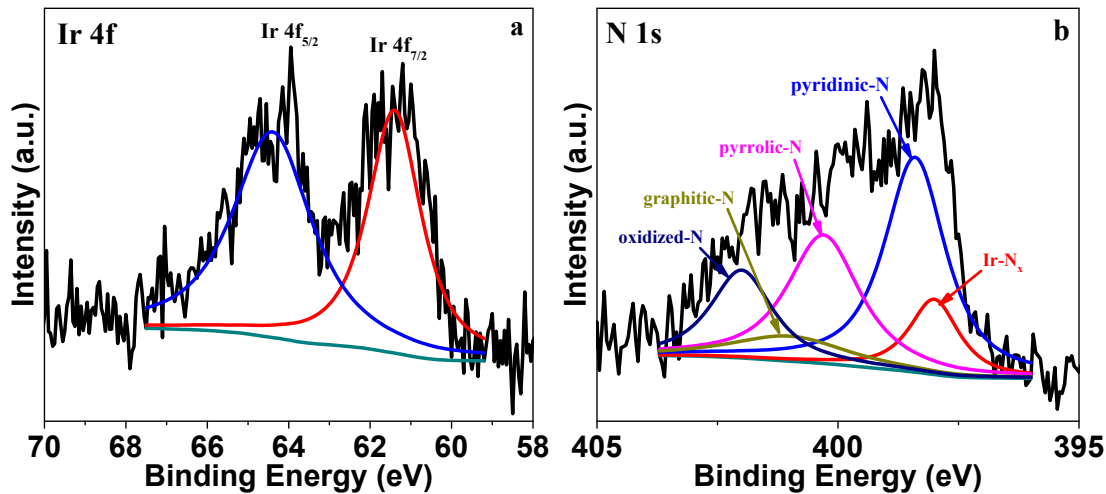


Figure S21. The high-resolution Ir4f (a) and N1s (b) XPS spectra of the used Ir@NG-750 catalyst after ORR test in 0.5 M H_2SO_4 .

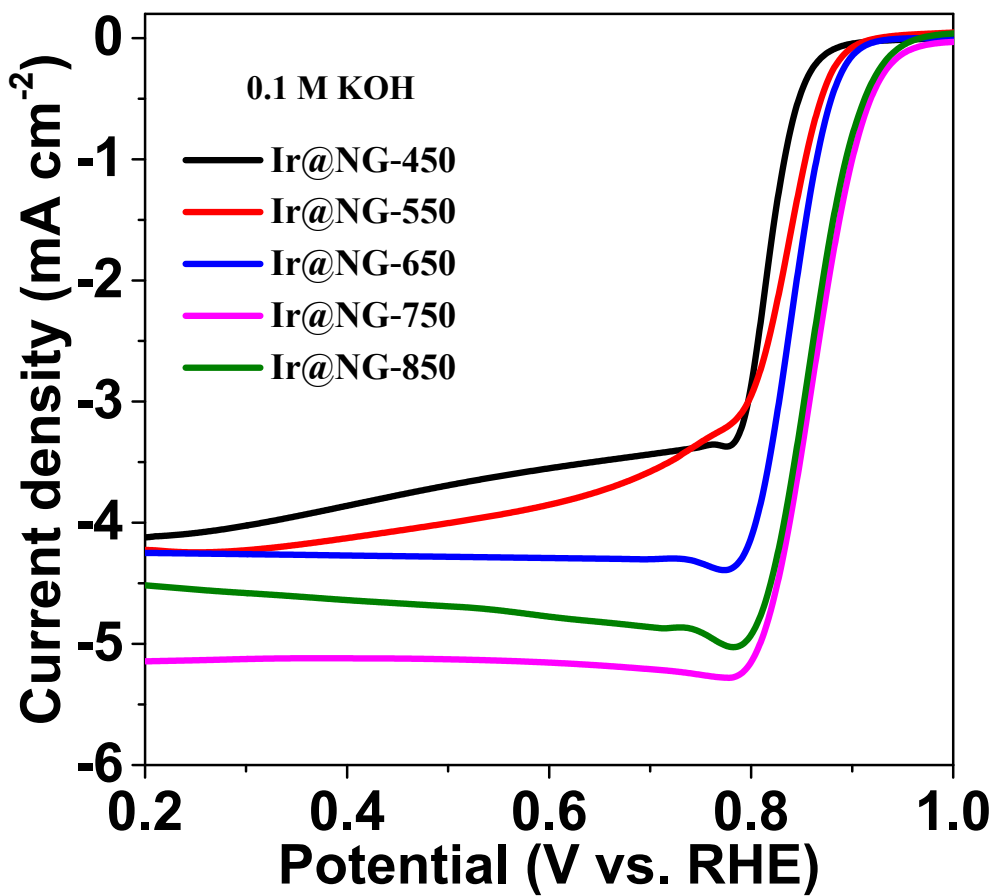


Figure S22. Polarization curves of 0.7-Ir@NG-T with different annealing temperature

at a rotation speed of 1600 rpm in 0.1 M KOH.

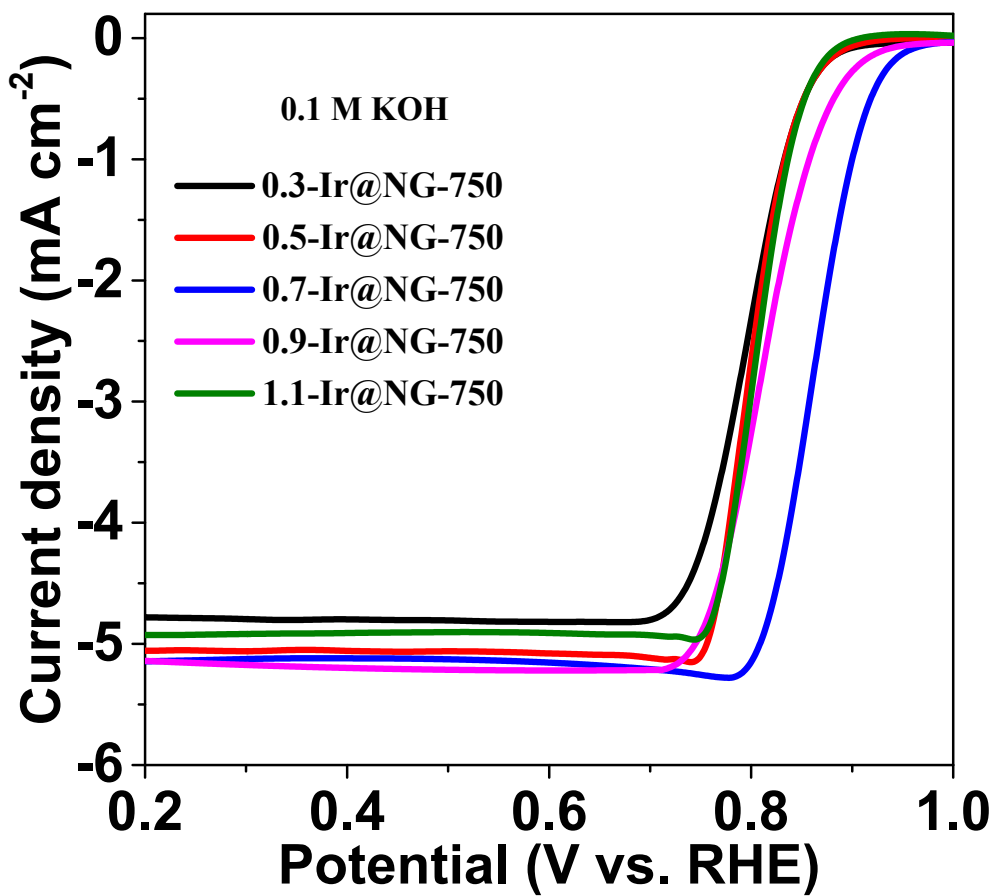


Figure S23. Polarization curves of Ir@NG-750 with different initial Ir content at a rotation speed of 1600 rpm in 0.1 M KOH.

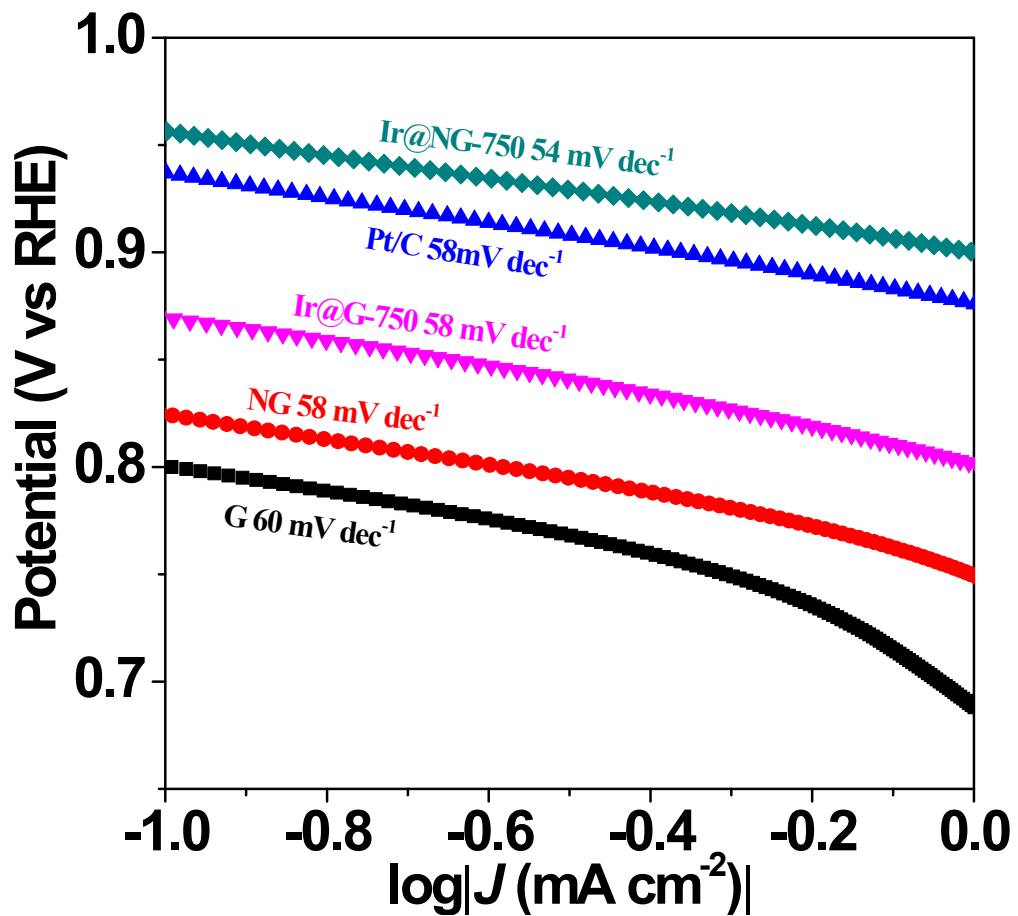


Figure S24. Tafel plots for Pt/C, G, NG, Ir@G-750, and Ir@NG-750 in 0.1 M KOH.

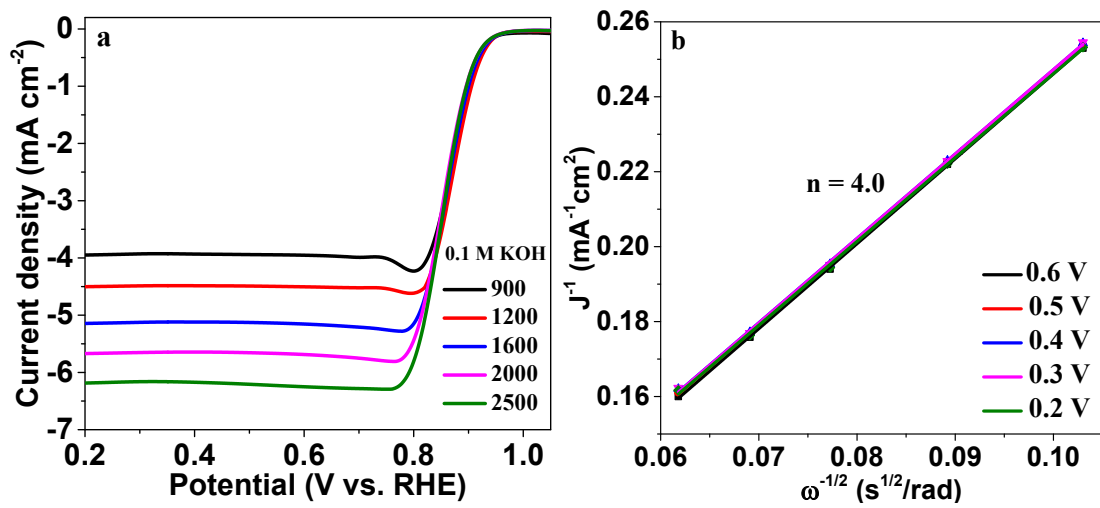


Figure S25. (a) Polarization curves of Ir@NG-750 at various rotation speeds in O_2 -saturated 0.1 M KOH . (b) The corresponding Koutecky–Levich plots.

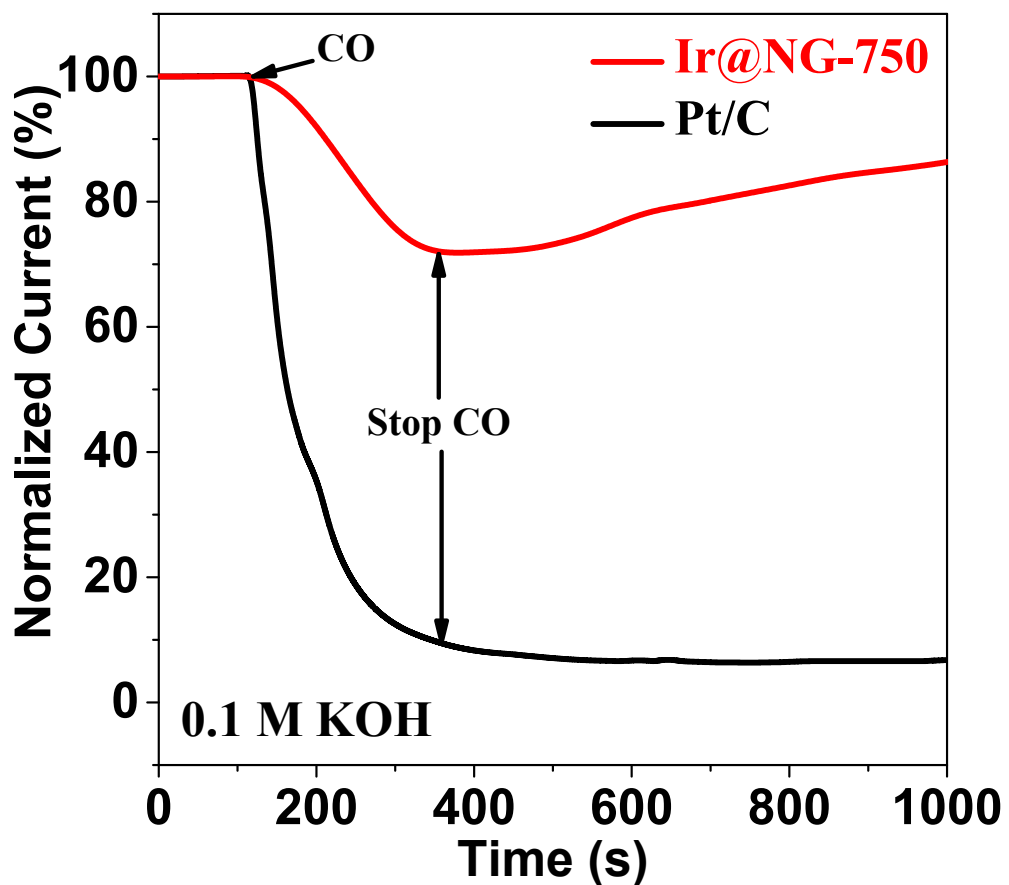


Figure S26. Tolerance to carbon monoxide of Ir@NG-750 compared with 20 wt% Pt/C in O₂-saturated 0.1 M KOH solution at 0.7 V vs RHE.

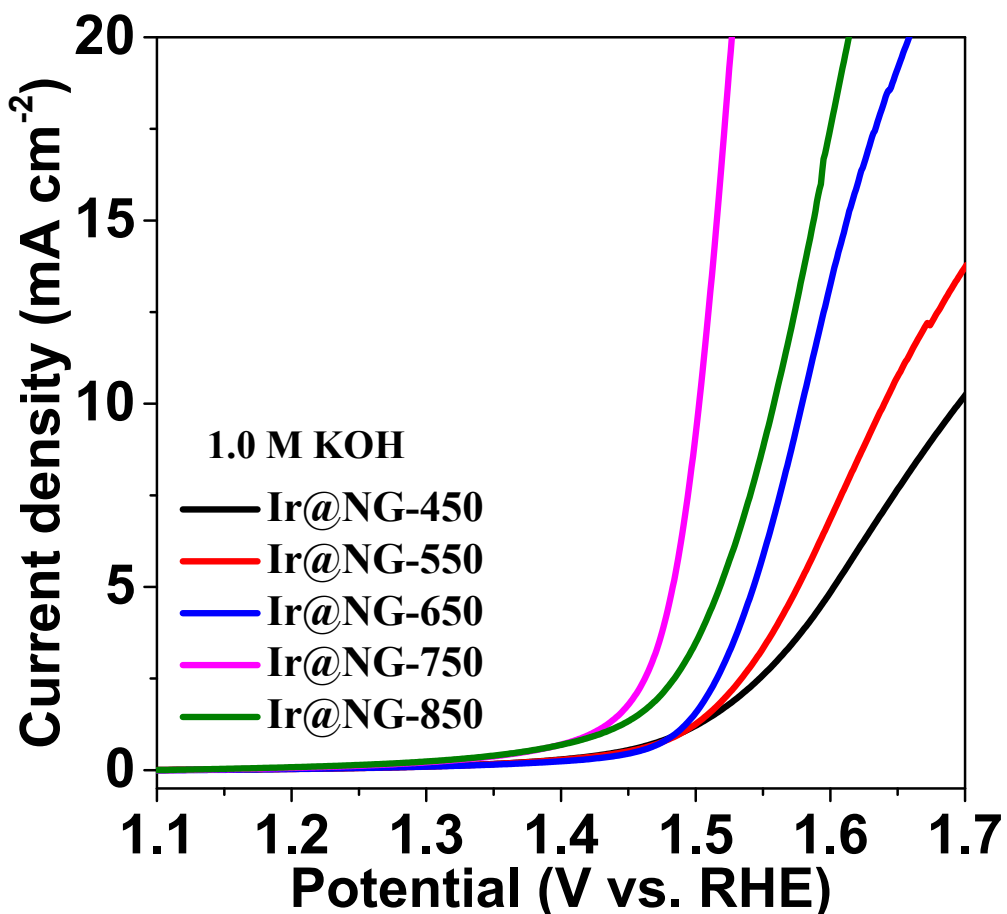


Figure S27. LSV curves of 0.7-Ir@NG-T with different annealing temperature in 1.0 M KOH.

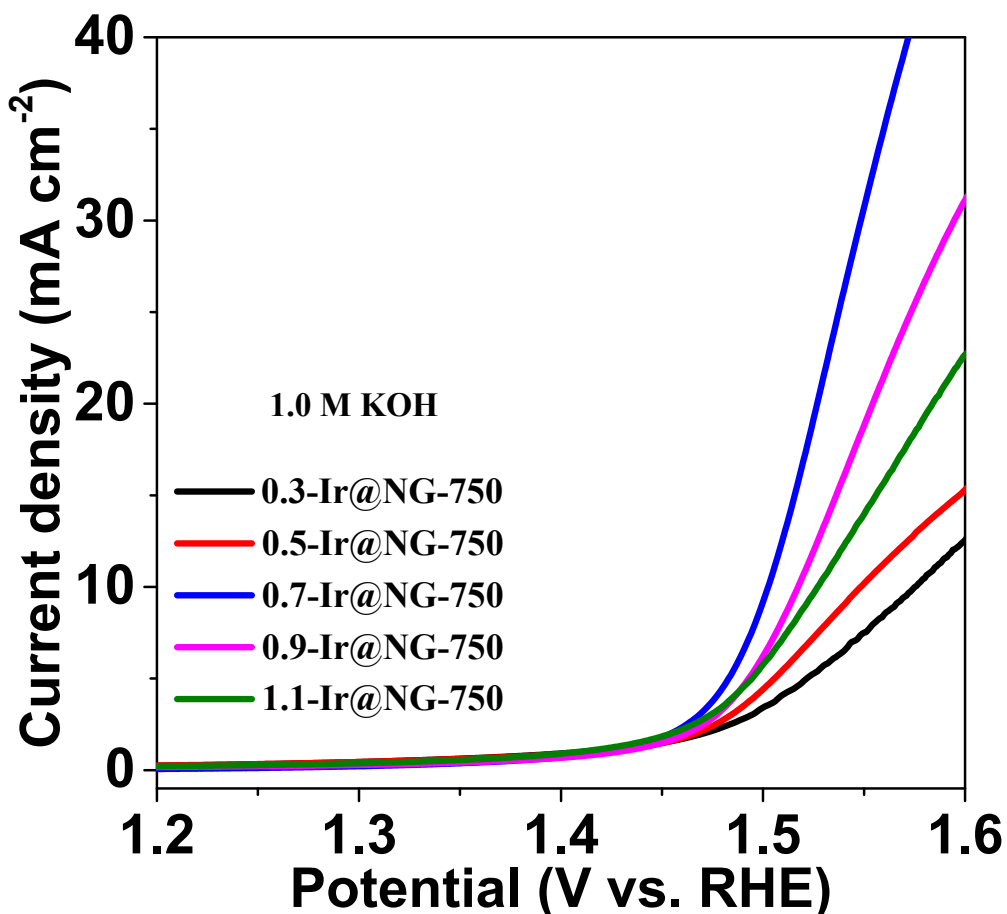


Figure S28. LSV curves of Ir@NG-750 with different initial Ir content in 1.0 M KOH.

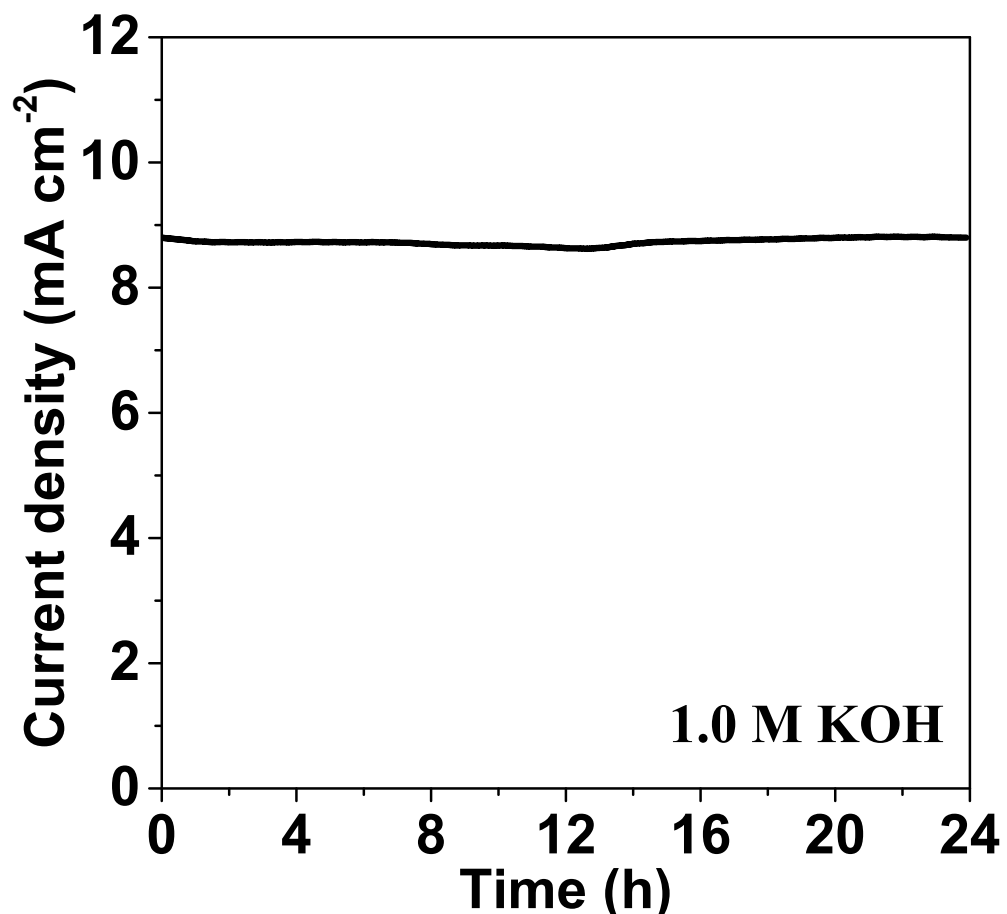


Figure S29. Plot of current density vs time for the Ir@NG-750 in-situ supported on graphite plate in 1.0 M KOH.

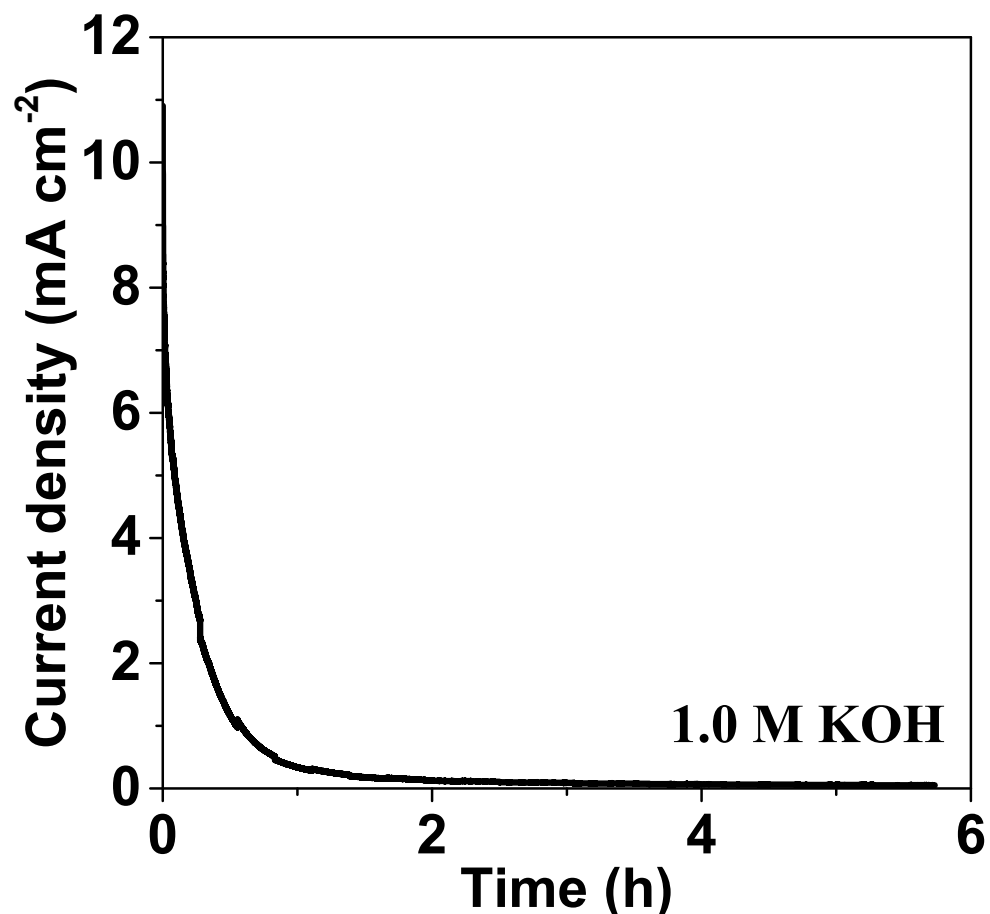


Figure S30. Plot of current density vs time for the IrO₂ nanoparticles in 1.0 M KOH.

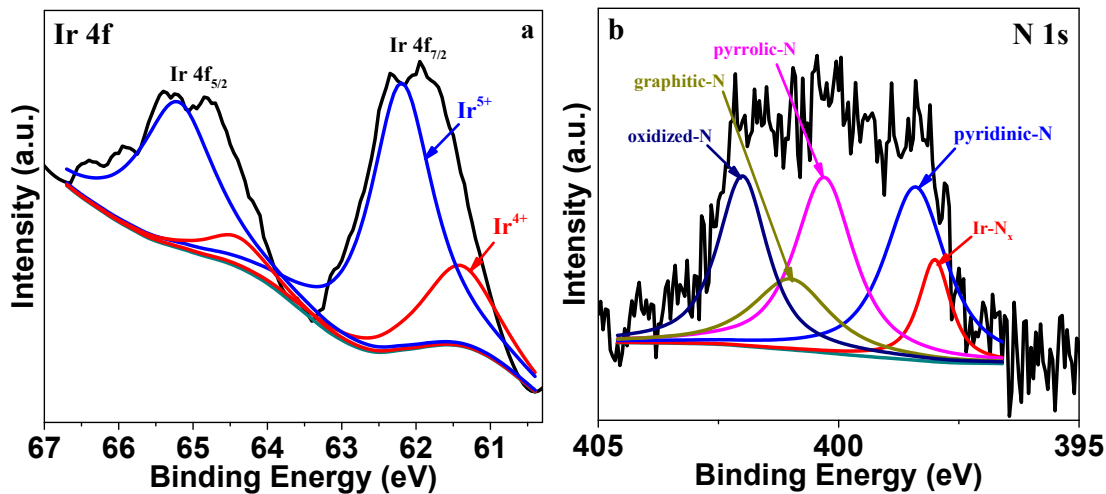


Figure S31. The high-resolution Ir4f (a) and N1s (b) XPS spectra of the used Ir@NG-750 catalyst after OER test in 1.0 M KOH.

Table S1. EXAFS data fitting result of Ir@NG-750

Sample	Ir-N/O		D.W.	ΔE
	R	CN		
Ir@NG-750	2.01 ± 0.01	5.1 ± 1.7	0.002 (O) 0.004 (Ir)	12

Table S2. Comparison of HER performance of Ir@NG-750 with results in recent literature

Catalyst	Electrolyte	$\eta @ 10 \text{ mA}\cdot\text{cm}^{-2}$ (mV)	Tafel slope (mV·dec ⁻¹)	Ref.
Ir@NG-750	0.5 M H ₂ SO ₄	25	14.8	This work
Ir@NG-750	0.1 M KOH	114	20.5	This work
Ir ₁ @Co/NC	1.0 M KOH	55	119	22
IrCo@NC	1.0 M KOH	45	23	23
Ru SAs@PN	0.5 M H ₂ SO ₄	24	28	24
Ru@Co-SAs/N-C	0.5 M H ₂ SO ₄	57	55	25
RuCo@NC	1.0 M KOH	28	31	26
Ru@NG-750	1.0 M KOH	40	35.9	27
Ni@Ni ₂ P–Ru	0.5 M H ₂ SO ₄	51	35	28
Ru/C ₃ N ₄ /C	0.1 M KOH	79	N.A.	29
RuP ₂ @NPC	1.0 M KOH	52	69	30
Ru/NC	1.0 M KOH	21	31	31
Pt ₁ /NPC	0.5 M H ₂ SO ₄	25	28	32
Pt-Ni nanowire	1.0 M KOH	50~60	N.A.	33
Pt-Ni alloy	0.1 M KOH	65	74	34
Ni _{SA} -MoS ₂ /CC	1.0 M KOH	95	75	35
Ni _{SA} -MoS ₂ /CC	0.5 M H ₂ SO ₄	110	74	35
MoC _x	1.0 M KOH	151	59	36
Co-NG	0.5 M H ₂ SO ₄	147	82	21
CoS ₂ HNSs	1.0 M KOH	193	100	37
Co-NRCNTs	0.5 M H ₂ SO ₄	260	69	38
CoSe ₂ MP/CC	0.5 M H ₂ SO ₄	193	50	39
Co@NC/NCNS-800	1.0 M KOH	219	55.8	40
Co ₃ S ₄ polyhedra	0.5 M H ₂ SO ₄	380	85.3	41
Co _{0.6} Mo _{1.4} N ₂	0.1 M KOH	320	80	42
CoP	0.1 M KOH	210	129	43
CoMoP NPs	0.5 M H ₂ SO ₄	178	60.5	44
Co@NiCoP	0.5 M H ₂ SO ₄	276	43	45

N.A.: the unknown data.

Table S3. Comparison of ORR performance of Ir@NG-750 with results in recent literature

Catalyst	Electrolyte	E _{onset} (V)	E _{1/2} (V)	Ref.
Ir@NG-750	0.5 M H ₂ SO ₄	0.846	0.77	This work
Ir@NG-750	0.1 M KOH	0.956	0.865	This work
Ir-SAC	0.1 M HClO ₄	0.97	0.864	⁴⁶
Fe-N _x ISAs/GHSs	0.1 M KOH	1.05	0.87	⁴⁷
Fe-N-C-900	0.1 M KOH	0.99	0.927	⁴⁸
Fe-NSDC	0.1 M KOH	0.96	0.84	⁴⁹
Fe-N-C HNSs	0.1 M KOH	1.046	0.87	⁵⁰
Fe-N-C900	0.1 M KOH	1.09	0.908	⁵¹
Fe-N-C900	0.5 M H ₂ SO ₄	0.962	0.795	⁵¹
FeN _x -PNC	0.1 M KOH	0.997	0.86	⁵²
CoSAs@CNTs	0.1 M KOH	0.99	0.86	⁵³
CoN ₄ /NG	0.1 M KOH	0.98	0.87	⁵⁴
CoNC700	0.1 M KOH	0.89	0.73	⁵⁵
CoNC700	0.1 M HClO ₄	0.96	0.85	⁵⁵
Ru@NG-750	0.1 M KOH	0.945	0.826	²⁷
Ru@NG-750	0.1 M HClO ₄	0.893	0.723	²⁷
Cr/N/C SACs	0.1 M HClO ₄	-	0.773	⁵⁶
Cu SAC	0.1 M KOH	0.97	0.81	⁵⁷
Cu@NG-750	0.1 M KOH	0.94	0.84	⁵⁸
Cu-SAs/N-C	0.1 M KOH	0.99	0.895	⁵⁹
ZnNCs	0.1 M KOH	-	0.857	⁶⁰
Sc@NG-750	0.1 M KOH	0.99	0.89	⁶¹
Sc@NG-750	0.5 M H ₂ SO ₄	0.82	0.72	⁶¹
Mn@NG	0.1 M KOH	0.95	0.82	⁶²
SW-N-C	0.1 M KOH	1.01	0.88	⁶³
SW-N-C	0.1 M HClO ₄	0.87	0.77	⁶³
(Fe,Co)/N-C	0.1 M HClO ₄	1.06	0.863	⁶⁴

Table S4. Comparison of OER performance of Ir@NG-750 with results in recent literature

Catalyst	Electrolyte	$\eta @ 10\text{mA}$ $\text{cm}^{-2} (\text{mV})$	Tafel slope (mV dec^{-1})	Ref.
Ir@NG-750	1.0 M KOH	273	64	This work
Ir@NG-750	0.1 M KOH	340	108	This work
Ir@NG-750	0.5 M H_2SO_4	371	104	This work
Ir ₁ @Co/NC	1.0 M KOH	260	163	22
CoIr-0.2	1.0 M KOH	235	70.2	65
FeN _x -PNC	0.1 M KOH	395	80	52
CoSAs@CNT	1.0 M KOH	410	85	53
S				
Co-NHGF	1.0 M KOH	402	80	66
CoN ₄ /NG	0.1 M KOH	380	81	54
UNT Co	0.1 M KOH	380	77	67
SAs/N-C				
SCoNC	0.1 M KOH	310	74	68
S NiN _x -PC/EG	1.0 M KOH	280	45	69
Ni,N-G	1.0 M KOH	270	59	70
Ru@NG-750	1.0 M KOH	372	68	27
Mn-NG	1.0 M KOH	337	55	71
Pt/NiO	1.0 M KOH	358	33	72
Au ₁ N _x /C ₃ N ₄	0.1 M KOH	450	112	73
NiFe-PCN	1.0 M KOH	310	38	74
CoDNI-N/C	0.1 M KOH	360	72	75

Table S5. Comparisons of Ir@NG-750 as bifunctional electrocatalysts for water splitting at 10 mA cm⁻² with others in alkaline media

Electrocatalyst	Potential (V vs. RHE)	Electrolyte	Reference
Ir@NG-750	1.7	1.0 M KOH	This work
Porous carbon clothes	1.85	1.0 M KOH	⁷⁶
Defect-rich porous carbon	1.74	1.0 M KOH	⁷⁷
Porous graphene nanosheets	1.91	1.0 M KOH	⁷⁸
N, S co-doped graphitic sheets	1.68	1.0 M KOH	⁷⁹
N, S co-doped carbon nanotubes	2.03	1.0 M KOH	⁸⁰
Ni ₅ P ₄ films	1.7	1.0 M KOH	⁸¹
CP/CTs/Co-S	1.74	1.0 M KOH	⁸²
NiFe LDHs/NF	1.7	1.0 M KOH	⁸³
Co–Fe oxyphosphide	1.69	1.0 M KOH	⁸⁴
Co ₅ Mo _{1.0} P NSS@NF	1.68	1.0 M KOH	⁸⁵

N.A.: the unknown data.

References

1. W. S. Hummers and R. E. Offeman, *J. Am. Chem. Soc.*, 1958, 80, 1339-1339.
2. G. Kresse and J. Hafner, *Phys. Rev. B*, 1993, 47, 558-561.
3. G. Kresse and J. Furthmuller, *Phys. Rev. B*, 1996, 54, 11169-11186.
4. J. P. Perdew, K. Burke and M. Ernzerhof, *Phys. Rev. Lett.*, 1996, 77, 3865-3868.
5. P. E. Blochl, *Phys. Rev. B*, 1994, 50, 17953-17979.
6. J. Heyd, G. E. Scuseria and M. Ernzerhof, *J. Chem. Phys.*, 2003, 118, 8207-8215.
7. A. V. Krukau, O. A. Vydrov, A. F. Izmaylov and G. E. Scuseria, *J. Chem. Phys.*, 2006, 125, 224106.
8. H. J. Monkhorst and J. D. Pack, *Phys. Rev. B*, 1976, 13, 5188-5192.
9. K. Mathew, R. Sundararaman, K. Letchworth-Weaver, T. Arias and R. G. Hennig, *J. Chem. Phys.*, 2014, 140, 084106.
10. J. K. Norskov, J. Rossmeisl, A. Logadottir, L. Lindqvist, J. R. Kitchin, T. Bligaard and H. Jonsson, *J. Phys. Chem. B*, 2004, 108, 17886-17892.
11. I. C. Man, H.-Y. Su, F. Calle-Vallejo, H. A. Hansen, J. I. Martinez, N. G. Inoglu, J. Kitchin, T. F. Jaramillo, J. K. Norskov and J. Rossmeisl, *ChemCatChem*, 2011, 3, 1159-1165.
12. H.-Y. Su, Y. Gorlin, I. C. Man, F. Calle-Vallejo, J. K. Norskov, T. F. Jaramillo and J. Rossmeisl, *Phys. Chem. Chem. Phys.*, 2012, 14, 14010-14022.
13. J. K. Nørskov, T. Bligaard, A. Logadottir, J. Kitchin, J. G. Chen, S. Pandelov

- and U. Stimming, *J. Electrochem. Soc.*, 2005, 152, J23-J26.
14. C. D. Taylor, S. A. Wasileski, J.-S. Filhol and M. Neurock, *Phys. Rev. B*, 2006, 73, 165402.
15. Z. Duan and G. Henkelman, *Langmuir*, 2018, 34, 15268-15275.
16. Z. Duan and G. Henkelman, *ACS Catal.*, 2019, 9, 5567-5573.
17. Y. Liang, Y. Li, H. Wang, J. Zhou, J. Wang, T. Regier and H. Dai, *Nat. Mater.*, 2011, 10, 780-786.
18. Y. Li, W. Zhou, H. Wang, L. Xie, Y. Liang, F. Wei, J.-C. Idrobo, S. J. Pennycook and H. Dai, *Nat. Nanotechnol.*, 2012, 7, 394-400.
19. M. B. Stevens, L. J. Enman, A. S. Batchellor, M. R. Cosby, A. E. Vise, C. D. M. Trang and S. W. Boettcher, *Chem. Mater.*, 2017, 29, 120-140.
20. J. Kibsgaard and T. F. Jaramillo, *Angew. Chem., Int. Ed.*, 2014, 53, 14433-14437.
21. H. Fei, J. Dong, M. J. Arellano-Jimenez, G. Ye, N. D. Kim, E. L. G. Samuel, Z. Peng, Z. Zhu, F. Qin, J. Bao, M. J. Yacaman, P. M. Ajayan, D. Chen and J. M. Tour, *Nat. Commun.*, 2015, 6, 8668.
22. W.-H. Lai, L.-F. Zhang, W.-B. Hua, S. Indris, Z.-C. Yan, Z. Hu, B. Zhang, Y. Liu, L. Wang, M. Liu, R. Liu, Y.-X. Wang, J.-Z. Wang, Z. Hu, H.-K. Liu, S.-L. Chou and S.-X. Dou, *Angew. Chem., Int. Ed.*, 2019, 58, 11868-11873.
23. P. Jiang, J. Chen, C. Wang, K. Yang, S. Gong, S. Liu, Z. Lin, M. Li, G. Xia and Y. Yang, *Adv. Mater.*, 2018, 30, 1705324.
24. J. Yang, B. Chen, X. Liu, W. Liu, Z. Li, J. Dong, W. Chen, W. Yan, T. Yao, X.

- Duan, Y. Wu and Y. Li, *Angew. Chem., Int. Ed.*, 2018, 57, 9495-9500.
25. S. Yuan, Z. Pu, H. Zhou, J. Yu, I. S. Amiinu, J. Zhu, Q. Liang, J. Yang, D. He, Z. Hu, G. Van Tendeloo and S. Mu, *Nano Energy*, 2019, 59, 472-480.
26. J. Su, Y. Yang, G. Xia, J. Chen, P. Jiang and Q. Chen, *Nat. Commun.*, 2017, 8, 14969.
27. L. Bai, Z. Duan, X. Wen, R. Si, Q. Zhang and J. Guan, *ACS Catal.*, 2019, 9, 9897-9904.
28. Y. Liu, S. Liu, Y. Wang, Q. Zhang, L. Gu, S. Zhao, D. Xu, Y. Li, J. Bao and Z. Dai, *J. Am. Chem. Soc.*, 2018, 140, 2731-2734.
29. Y. Zheng, Y. Jiao, Y. Zhu, L. H. Li, Y. Han, Y. Chen, M. Jaroniec and S.-Z. Qiao, *J. Am. Chem. Soc.*, 2016, 138, 16174-16181.
30. Z. Pu, I. S. Amiinu, Z. Kou, W. Li and S. Mu, *Angew. Chem., Int. Ed.*, 2017, 56, 11559-11564.
31. J. Zhang, P. Liu, G. Wang, P. Zhang, X. Zhuang, M. Chen, I. Weidinger and X. Feng, *J. Mater. Chem. A*, 2017, 5, 25314-25318.
32. T. Li, J. Liu, Y. Song and F. Wang, *ACS Catal.*, 2018, 8, 8450-8458.
33. P. Wang, X. Zhang, J. Zhang, S. Wan, S. Guo, G. Lu, J. Yao and X. Huang, *Nat. Commun.*, 2017, 8, 14580.
34. Z. Cao, Q. Chen, J. Zhang, H. Li, Y. Jiang, S. Shen, G. Fu, B.-a. Lu, Z. Xie and L. Zheng, *Nat. Commun.*, 2017, 8, 15131.
35. Q. Wang, Z. L. Zhao, S. Dong, D. He, M. J. Lawrence, S. Han, C. Cai, S. Xiang, P. Rodriguez, B. Xiang, Z. Wang, Y. Liang and M. Gu, *Nano Energy*,

- 2018, 53, 458-467.
36. H. B. Wu, B. Y. Xia, L. Yu, X.-Y. Yu and X. W. Lou, *Nat. Commun.*, 2015, 6, 6512.
37. X. Ma, W. Zhang, Y. Deng, C. Zhong, W. Hu and X. Han, *Nanoscale*, 2018, 10, 4816-4824.
38. X. Zou, X. Huang, A. Goswami, R. Silva, B. R. Sathe, E. Mikmekova and T. Asefa, *Angew. Chem., Int. Ed.*, 2014, 53, 4372-4376.
39. Q. Liu, J. Shi, J. Hu, A. M. Asiri, Y. Luo and X. Sun, *ACS Appl. Mater. Interf.*, 2015, 7, 3877-3881.
40. M. Li, T. Liu, X. Bo, M. Zhou and L. Guo, *J. Mater. Chem. A*, 2017, 5, 5413-5425.
41. Z.-F. Huang, J. Song, K. Li, M. Tahir, Y.-T. Wang, L. Pan, L. Wang, X. Zhang and J.-J. Zou, *J. Am. Chem. Soc.*, 2016, 138, 1359-1365.
42. R. Subbaraman, D. Tripkovic, K.-C. Chang, D. Strmcnik, A. P. Paulikas, P. Hirunsit, M. Chan, J. Greeley, V. Stamenkovic and N. M. Markovic, *Nat. Mater.*, 2012, 11, 550-557.
43. J. Tian, Q. Liu, A. M. Asiri and X. Sun, *J. Am. Chem. Soc.*, 2014, 136, 7587-7590.
44. Y.-Y. Ma, C.-X. Wu, X.-J. Feng, H.-Q. Tan, L.-K. Yan, Y. Liu, Z.-H. Kang, E.-B. Wang and Y.-G. Li, *Energy Environ. Sci.*, 2017, 10, 788-798.
45. Y. Bai, H. Zhang, L. Liu, H. Xu and Y. Wang, *Chem.-Eur. J.*, 2016, 22, 1021-1029.

46. M. Xiao, J. Zhu, G. Li, N. Li, S. Li, Z. P. Cano, L. Ma, P. Cui, P. Xu, G. Jiang, H. Jin, S. Wang, T. Wu, J. Lu, A. Yu, D. Su and Z. Chen, *Angew. Chem., Int. Ed.*, 2019, 58, 9640-9645.
47. X. Qiu, X. Yan, H. Pang, J. Wang, D. Sun, S. Wei, L. Xu and Y. Tang, *Adv. Sci. (Weinheim, Ger.)*, 2019, 6.
48. C. Zhu, Q. Shi, B. Z. Xu, S. Fu, G. Wan, C. Yang, S. Yao, J. Song, H. Zhou, D. Du, S. P. Beckman, D. Su and Y. Lin, *Adv. Energy Mater.*, 2018, 8.
49. J. Zhang, M. Zhang, Y. Zeng, J. Chen, L. Qiu, H. Zhou, C. Sun, Y. Yu, C. Zhu and Z. Zhu, *Small*, 2019, 15, 1900307.
50. Y. Chen, Z. Li, Y. Zhu, D. Sun, X. Liu, L. Xu and Y. Tang, *Adv. Mater.*, 2019, 31, 1806312.
51. D. Lyu, Y. B. Mollamahale, S. Huang, P. Zhu, X. Zhang, Y. Du, S. Wang, M. Qing, Z. Q. Tian and P. K. Shen, *J. Catal.*, 2018, 368, 279-290.
52. L. Ma, S. Chen, Z. Pei, Y. Huang, G. Liang, F. Mo, Q. Yang, J. Su, Y. Gao and J. A. Zapien, *ACS Nano*, 2018, 12, 1949-1958.
53. S. Dilpazir, H. He, Z. Li, M. Wang, P. Lu, R. Liu, Z. Xie, D. Gao and G. Zhang, *ACS Appl. Energy Mater.*, 2018, 1, 3283-3291.
54. L. Yang, L. Shi, D. Wang, Y. Lv and D. Cao, *Nano Energy*, 2018, 50, 691-698.
55. G. Wan, P. Yu, H. Chen, J. Wen, C.-j. Sun, H. Zhou, N. Zhang, Q. Li, W. Zhao, B. Xie, T. Li and J. Shi, *Small*, 2018, 14.
56. E. Luo, H. Zhang, X. Wang, L. Gao, L. Gong, T. Zhao, Z. Jin, J. Ge, Z. Jiang, C. Liu and W. Xing, *Angew. Chem., Int. Ed.*, 2019, 58, 12469-12475.

57. L. Cui, L. Cui, Z. Li, J. Zhang, H. Wang, S. Lu and Y. Xiang, *J. Mater. Chem. A*, 2019, 7, 16690-16695.
58. L. Bai, C. Hou, X. Wen and J. Guan, *ACS Appl. Energy Mater.*, 2019, 2, 4755-4762.
59. Y. Qu, Z. Li, W. Chen, Y. Lin, T. Yuan, Z. Yang, C. Zhao, J. Wang, C. Zhao, X. Wang, F. Zhou, Z. Zhuang, Y. Wu and Y. Li, *Nat. Catal.*, 2018, 1, 781-786.
60. F. Li, Y. Bu, G.-F. Han, H.-J. Noh, S.-J. Kim, I. Ahmad, Y. Lu, P. Zhang, H. Y. Jeong, Z. Fu, Q. Zhong and J.-B. Baek, *Nat. Commun.*, 2019, 10, 2623.
61. X. Wen, Z. Duan, L. Bai and J. Guan, *J. Power Sources*, 2019, 431, 265-273.
62. L. Bai, Z. Duan, X. Wen, R. Si and J. Guan, *Appl. Catal. B: Environ.*, 2019, 257, 117930.
63. Z. Chen, W. Gong, Z. Liu, S. Cong, Z. Zheng, Z. Wang, W. Zhang, J. Ma, H. Yu, G. Li, W. Lu, W. Ren and Z. Zhao, *Nano Energy*, 2019, 60, 394-403.
64. J. Wang, Z. Huang, W. Liu, C. Chang, H. Tang, Z. Li, W. Chen, C. Jia, T. Yao, S. Wei, Y. Wu and Y. Li, *J. Am. Chem. Soc.*, 2017, 139, 17281-17284.
65. Y. Zhang, C. Wu, H. Jiang, Y. Lin, H. Liu, Q. He, S. Chen, T. Duan and L. Song, *Adv. Mater.*, 2018, 30, 1707522.
66. H. Fei, J. Dong, Y. Feng, C. S. Allen, C. Wan, B. Voloskiy, M. Li, Z. Zhao, Y. Wang and H. Sun, *Nat. Catal.*, 2018, 1, 63-72.
67. X. Sun, S. Sun, S. Gu, Z. Liang, J. Zhang, Y. Yang, Z. Deng, P. Wei, J. Peng and Y. Xu, *Nano Energy*, 2019, 61, 245-250.
68. J. Wu, H. Zhou, Q. Li, M. Chen, J. Wan, N. Zhang, L. Xiong, S. Li, B. Y. Xia,

- G. Feng, M. Liu and L. Huang, *Adv. Energy Mater.*, 2019, 9, 1900149.
69. Y. Hou, M. Qiu, M. G. Kim, P. Liu, G. Nam, T. Zhang, X. Zhuang, B. Yang, J. Cho, M. Chen, C. Yuan, L. Lei and X. Feng, *Nat. Commun.*, 2019, 10, 1392.
70. H. J. Qiu, P. Du, K. Hu, J. Gao, H. Li, P. Liu, T. Ina, K. Ohara, Y. Ito and M. Chen, *Adv. Mater.*, 2019, 31, 1900843.
71. J. Guan, Z. Duan, F. Zhang, S. D. Kelly, R. Si, M. Dupuis, Q. Huang, J. Q. Chen, C. Tang and C. Li, *Nat. Catal.*, 2018, 1, 870-877.
72. C. Lin, Y. Zhao, H. Zhang, S. Xie, Y.-F. Li, X. Li, Z. Jiang and Z.-P. Liu, *Chem. Sci.*, 2018, 9, 6803-6812.
73. L. Liu, H. Su, F. Tang, X. Zhao and Q. Liu, *Nano Energy*, 2018, 46, 110-116.
74. C. Wu, X. Zhang, Z. Xia, M. Shu, H. Li, X. Xu, R. Si, A. I. Rykov, J. Wang and S. Yu, *J. Mater. Chem. A*, 2019, 7, 14001-14010.
75. Z. Li, H. He, H. Cao, S. Sun, W. Diao, D. Gao, P. Lu, S. Zhang, Z. Guo, M. Li, R. Liu, D. Ren, C. Liu, Y. Zhang, Z. Yang, J. Jiang and G. Zhang, *Appl. Catal. B: Environ.*, 2019, 240, 112-121.
76. M.-S. Balogun, W. Qiu, H. Yang, W. Fan, Y. Huang, P. Fang, G. Li, H. Ji and Y. Tong, *Energy Environ. Sci.*, 2016, 9, 3411-3416.
77. Z. Zhang, Z. Yi, J. Wang, X. Tian, P. Xu, G. Shi and S. Wang, *J. Mater. Chem. A*, 2017, 5, 17064-17072.
78. X. Yue, S. Huang, J. Cai, Y. Jin and P. K. Shen, *J. Mater. Chem. A*, 2017, 5, 7784-7790.
79. C. Hu and L. Dai, *Adv. Mater.*, 2017, 29, 1604942.

80. K. Qu, Y. Zheng, Y. Jiao, X. Zhang, S. Dai and S. Z. Qiao, *Adv. Energy Mater.*, 2017, 7, 1602068.
81. M. Ledendecker, S. K. Calderon, C. Papp, H.-P. Steinrueck, M. Antonietti and M. Shalom, *Angew. Chem., Int. Ed.*, 2015, 54, 12361-12365.
82. J. Wang, H.-x. Zhong, Z.-l. Wang, F.-l. Meng and X.-b. Zhang, *ACS Nano*, 2016, 10, 2342-2348.
83. J. Luo, J.-H. Im, M. T. Mayer, M. Schreier, M. K. Nazeeruddin, N.-G. Park, S. D. Tilley, H. J. Fan and M. Grätzel, *Science*, 2014, 345, 1593-1596.
84. P. Zhang, X. F. Lu, J. Nai, S.-Q. Zang and X. W. Lou, *Adv. Sci. (Weinheim, Ger.)*, 2019, DOI: 10.1002/advs.201900576, 1900576.
85. Y. Zhang, Q. Shao, S. Long and X. Huang, *Nano Energy*, 2018, 45, 448-455.